Global and Planetary Change 217 (2022) 103929

Contents lists available at ScienceDirect

Global and Planetary Change

journal homepage: www.elsevier.com/locate/gloplacha

Role of crustal fluids and thermo-mechanical structure for lower crustal seismicity: The Gargano Promontory (southern Italy)

Alessio Lavecchia [a,b,*], Marilena Filippucci [a], Andrea Tallarico [a], Giulio Selvaggi [b], Gianpaolo Cecere [b], Sierd Cloetingh [c]

[a] Dipartimento di Scienze della Terra e Geoambientali, Universita di Bari - Aldo Moro, Bari, Italy
[b] Istituto Nazionale di Geofisica e Vulcanologia - Sede Irpinia, Grottaminarda, Italy
[c] Department of Earth Sciences, Utrecht University, Utrecht, the Netherlands

ARTICLE INFO

Editor: Zhengtang Guo

Keywords:
Lower crust
Seismology
Rheology
Geotherm
Numerical modeling
Gargano Promontory (southern Italy)

ABSTRACT

Several regions around the globe are characterized by a seismically active lower crust, at depths where lithological and thermal conditions suggest stress release by ductile flow. The Gargano Promontory (GP, southern Italy) is an example where a recently installed seismic network has recorded an intense seismic activity at depths between 20 and 30 km, i.e. in the lower crust. The GP is located in proximity of the Gargano-Dubrovnik lineament, a seismogenic zone separating the central and southern Adriatic basins. These two basins constitute sites of sediments accumulation since Tertiary times. Another important basin in the region is represented by the Apennine foredeep, that includes the Candelaro area. We analyze the possible mechanisms controlling the distribution of seismicity in the GP to identify the factors that make the lower crust seismically active. To this aim, we construct a thermo-rheological model of a layered continental crust, calibrated on the basis of geometrical, lithological and thermal constraints. The model takes into account various crustal lithologies, the presence of fluids in the crystalline basement, lateral variations of geotherm and stress field. The numerical simulations show that the presence of fluids is a key factor controlling the cluster of seismicity in the lower crust. Moreover, the presence of water in the upper crystalline basement and sedimentary cover provides a plausible explanation for upper crustal seismicity in a zone of very high heat flow SW of the GP. The distribution of the seismicity is probably affected by the composition of the crystalline basement, with mafic bodies injected into the crust during the Paleocene magmatic phase that affected the Mediterranean region. In addition, fluid accumulation and overpressure may occur along detachment levels in the lower crust, leading to clustering of the earthquakes. Based on our findings, we hypothesize that the presence of hydrous diapiric upwelling(s) in the upper mantle can feed a deep fluid circulation system, inducing lower crustal seismicity.

1. Introduction

The continental lower crust has historically been considered a weak layer, transferring stresses between the brittle upper crust and the lithospheric mantle via ductile flow (Burov, 2011). In this framework, the lack of seismicity is one of the main features of the lower crust. Earthquake hypocenters are not frequently detected in the lower crust and the correlation between depth of crustal seismicity, temperature and rock deformation mechanisms has led to the common view that the lower continental crystalline basement is in a ductile regime (Chen and Molnar, 1983). This is true in many continental areas, especially where the geothermal gradient is particularly high, as for instance in the Pannonian Basin of central Europe (Cloetingh and Burov, 1996; Lenkey et al., 2002). On the other hand, recent studies demonstrate that seismicity nucleated in the continental lower crust occurs in several locations around the globe (e.g. Simpson, 1999), including some major rift zones, such as the East African rift (Shudofsky et al., 1987; Craig and Jackson, 2021; Muluneh et al., 2021), Baikal rift (Déverchère et al., 2001; Radziminovich et al., 2013), Rhine rift (Deichmann, 1992; Anikiev et al., 2020, and references therein) and the Dead Sea rift (Aldersons et al., 2003; Salamon et al., 2003; Hofstetter et al., 2012).

The causes behind the nucleation of earthquakes in the lower crust are still a matter of an intense debate (e.g. Simpson, 1999; Campbell et al., 2020). The most common proposed mechanisms so far include

* Corresponding author at: Istituto Nazionale di Geofisica e Vulcanologia - Sede Irpinia, Grottaminarda, Italy.
E-mail address: alessio.lavecchia@ingv.it (A. Lavecchia).

https://doi.org/10.1016/j.gloplacha.2022.103929
Received 17 March 2022; Received in revised form 8 August 2022; Accepted 29 August 2022
Available online 6 September 2022

thermal-runaway plastic instability, dehydration reactions with subsequent increase in fluid pressure, local stress redistribution, transient high differential stress values and eclogitisation reactions (Campbell et al., 2020, and references therein).Fluid presence and circulation in the lower crust is one of the mechanisms that may promote seismicity (e.g. Audin et al., 2002; Gardonio et al., 2018; Benson et al., 2020, and references therein). In this context, it is of particular importance to distinguish between short-term and long-term effects of fluids on host rocks. The former is mostly mechanical and the presence of interconnected fluid phases decreases the shear stress needed to produce rock failure, favoring the likelihood of faulting and sliding (e.g. Ranalli, 1995; El Hariri et al., 2010; Van Dinther et al., 2013). On the other hand, on a longer time scale, host rocks can be subjected to hydrolithic weakening effects and therefore their strength can be significantly reduced (Tullis and Yund, 1989; Girard et al., 2013). Furthermore, fluids can exert a long term chemical effect by triggering metamorphic reactions and producing rheologically weaker rocks where deformation will mostly occur by viscous creep (e.g. Jamtveit et al., 2019; Wang et al., 2020). This is especially true for water, whereas the effect of CO2 on host rocks is more controversial (e.g. Chernak et al., 2009). Therefore, the study of fluid-crust interaction is pivotal to assess the seismic hazard in seismically active regions. In addition, fluids in the continental crust can form pore networks along grain edges and fluid percolation by either porous flow or surface energy-driven infiltration can affect electrical and thermal properties in the lower crust (e.g. Watson and Brenan, 1987). These mechanisms are preferably localized in the lower crust within shear zones, where creep cavitation and subgrain rotation recrystallization during mylonite formation lead to increased porosity (Menegon et al., 2015; Gilgannon et al., 2020).

One of the areas where seismicity has been detected in the lower crust is the Gargano Promontory (GP) of southern Italy. The GP is located in proximity of the Gargano-Dubrovnik lineament, a zone that separates the central and southern Adriatic basins (Oldow et al., 2002), formed in Neogene to Quaternary times and both characterized by strong crustal subsidence (Bertotti et al., 2001). Overall, the Adriatic plate is the site of very significant accumulations of Tertiary to Quaternary sediments that can be classified in three main sedimentary basins: the Apennine foredeep, that includes the Candelaro area and is adjacent to the Mesozoic carbonates (e.g. Murge limestones and GP) outcropping in the NE, the central Adriatic basin, located N of the GP, and the South Adriatic basin, located NE of the GP. The central and south basins' geometries and subsidence patterns point out that the Adriatic crust has undergone episodes of lithospheric buckling (Cloetingh and Burov, 2011) at least since Miocene. Specifically, in the GP the inversion of pre-existing, steep normal faults led to a first phase of vertical movements, followed by a major phase of shortening that began in the Langhian and ended before the middle-late Pliocene (Bertotti et al., 1999). Inversion of extensional basins, reactivation of pre-existing faults and upthrusting of crustal blocks are common features in orogenic evolution, as in the case of collisional coupling between Alpine and Pyrenean orogens with their forelands (e.g. Ziegler et al., 1995, and references therein) and can occur at notable distance, constituting a mechanism for intraplate deformation (Ziegler et al., 1998). This occurs also in areas adjacent to GP, where the late Pliocene to late Quaternary tectonic activity consists of forelandward propagation of the Apennine detachment, involving the inversion of inherited structures rooted in the basement (Scrocca et al., 2007). The GP is historically characterized by earthquakes with magnitude $M_w < 6.5$, some of them associated with

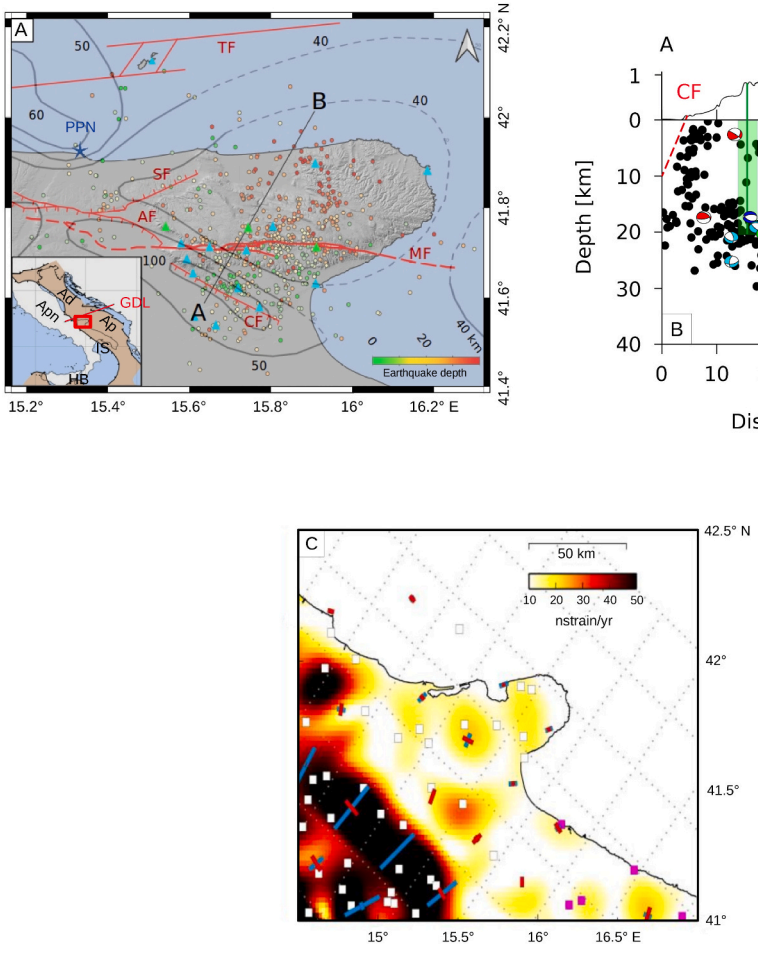

Fig. 1. A) Map of the Gargano promontory. Inset shows its location (red square) with respect to the Adria and Apulian microplates (brown area, Ad = Adria microplate, Ap = Apulian microplate, Apn = Apennines, HB=Hyblean block, IS=Ionian Sea) (D'Agostino et al., 2008); the red segment is the Gargano-Dubrovnik lineament (GDL) (after Battaglia et al., 2004). Earthquakes are indicated by small circles colored according to depth (Miccolis et al., 2021). Triangles represent the GSN network seismic stations (IV: blue, OT: green). Grey lines are the isolines of surface heat flow (mW m^{-2}) (Della Vedova et al., 2001). Red lines are the main faults (AF = Apricena Fault; CF=Candelaro Fault; MF = Mattinata Fault; SF=Sannicandro Fault; TF = Tremiti Fault, modified from Miccolis et al. (2021)). Blue star indicates Punta delle Pietre Nere (PPN). The A-B black segment is the trace of the vertical crustal section in panel A and B. B) Vertical cross-section along the A-B section: hypocenters (black circles) and focal mechanisms are projected over the vertical plane (red = normal; green = transcurrent; light blue = transpressive; dark blue = compressive; black = unknown). Red line indicates the CF, green line and green area indicate the MF fractured zone (after Miccolis et al. (2021)). C) Map of strain rate in the GP and surrounding areas, calculated from GPS data Cecere (2018). (For interpretation of the references to color in this figure legend, the reader is referred to the web version of this article.)

two main *E*-W fault systems: the Mattinata Fault and the Tremiti Fault (Del Gaudio et al., 2007). Until 2013, only two seismic stations of the Italian National Seismic Network (international code IV) were operating on the GP (MSAG, SGRT) (Fig. 1A). As a consequence, a high degree of inaccuracy was unavoidable in the detection and localization of the GP earthquakes. The seismic coverage of the region was largely improved with the installation of the OTRIONS seismic network (international code OT) in 2013. This network includes 12 seismic stations, equipped with a short-period Lennartz 3D-V seismometer and a 24-bit SL06/SARA data-logger. In June 2015 two of these stations were moved northward, improving the seismic monitoring of the norther part of the GP. Since January 2019, all the waveform data and station metadata are archived and distributed by the INGV node of EIDA (see Filippucci et al., 2021b, for further details). Stations of OT network and of IV network co-work to form the Gargano Seismic Network (GSN in Fig. 1A).

A comprehensive, high quality seismic catalogue of 635 earthquakes has been produced by merging several event databases (de Lorenzo et al., 2017; Filippucci et al., 2021b) and relocating the catalogues using the 1D velocity model of the GP (de Lorenzo et al., 2017). Earthquake locations have an average horizontal error of 0.5 km and an average vertical error of 0.6 km, with average residuals of 0.2 s. Earthquakes have local vertical magnitude Mlv ranging between 0.1 and 2.8 and local magnitude Ml between 0.5 and 3.6, with two exceptions of major earthquakes (April 23, 2017, Mlv = 4.0 and April 18, 2020, Ml = 3.7), and the 90% of earthquakes with Ml and Mlv < 2.0 (see Miccolis et al., 2021, for further details).This recorded seismicity (Filippucci et al., 2019a,b, 2021a,b; Miccolis et al., 2021) highlights an intense micro-earthquake activity in the whole GP at depths greater than 20 km (Fig. 1B). Hypocenters gently deepen toward the NE reaching depths of about 30 km (Fig. 1B). Focal mechanisms of earthquakes occurring in the NE part of the GP show thrust faulting kinematics (Filippucci et al., 2020; Miccolis et al., 2021). Conversely, seismic activity SW of the GP is markedly shallower and less intense, following a high angle lineament with maximum depth around 20 km and affecting an area located along the Candelaro Fault (CF in Fig. 1B), with focal mechanisms showing normal faulting kinematics. Previous studies of these two lineaments suggest that they are not part of a single major structure, but rather two distinct structures with different genesis and characteristics (Filippucci et al., 2021b; Miccolis et al., 2021). Microseismicity in the region is associated with very low values of strain rate at the surface. On the basis of GPS data in the GP, estimates for strain rate in the promontory are lower than the ones in the Apennines of around one magnitude order (Fig. 1C, Cecere, 2018).

A very high surface heat flow is measured in the CF area where this shallow seismicity is observed, with values that may exceed 100 mW m^{-2} (Fig. 1A). In this area the presence of water in crustal rocks has been observed (Tripaldi, 2020). Therefore, the high surface heat flow has been attributed to thermal conductivity increase and heat transport at shallow depth in the sedimentary cover due to fluid circulation (Della Vedova et al., 2001). On the other side, fluid presence at greater depth has not been unambiguously identified (Tripaldi, 2020).

A first attempt to study the GP crustal rheology was conducted by Dragoni et al. (1996) with an analytical 1D model. In this study a temperature-dependent viscosity was implemented and a transcurrent stress field and an average surface heat flow of 60 mWm^{-2} were adopted for the area. Recently this model was updated by Filippucci et al. (2019b), utilizing the heat flow map of Della Vedova et al. (2001) and subdividing the GP area in two different surface heat flow zones.

In this paper we present a numerical 2D thermo-rheological model, taking into account the effects of thermal, lithological and tectonic variations, both lateral and vertical, on rock strength with pore fluid pressure under hydrostatic and near-lithostatic conditions, adopting the GP as a test bed. This approach allows us to evaluate the rheological effect of lithology, cohesion loss and fluid presence, and implications for seismicity and surface heat flow in the region. With our model we calculate thermal structure and brittle-ductile strength distribution in 2D, in order to better understand what are the factors leading to a brittle behavior of the GP crust and therefore to generation of seismicity during plastic deformation. We show that earthquake clusters at lower crustal depths are probably triggered by high pore fluid pressure, in combination with the presence of mafic bodies injecting the crystalline basement.

2. Tectonic framework

The GP is part of the Adria platform (Fig. 1A), a region that constitutes the foreland-foredeep area of three orogenic systems: Alps to the N, Apennines to the W and Dinarides to the E (e.g. D'Agostino et al., 2008, and references therein). During the Eurasia-Africa convergence, the Adria plate acted as an indenter (Aliaj, 2006; Stein and Sella, 2006) and moved coherently with the African plate at least until late Miocene (Babbucci et al., 2004). Subsequently, the development of the westward Anatolian-Aegean-Balkan system resulted in decoupling of Adria from the Africa plate and a clockwise rotation of Adria with respect to Eurasia. As a consequence of this event, Adria movement changed to a counterclockwise rotation during late Pliocene to early Pleistocene, due to the plate collision with the southern parts of the Apennines (D'Agostino et al., 2008, and references therein). Although the current plate configuration in the Adria region is still controversial, recent studies suggest that Adria is today separated in two blocks along the Gargano-Dubrovnik lineament (Fig. 1A) (Oldow et al., 2002). Seismological and geodetic studies point out that at present day the Apulian sector moves independently from northern Adria, in a framework where Apulia moves coherently with the Ionian Sea and the Hyblean block (D'Agostino et al., 2008). The separation between Adria and Africa has been identified along the Apulian Escarpment (e.g. Battaglia et al., 2004) or alternatively in a region of diffuse deformation in the Ionian Sea (Stein and Sella, 2006).

In this framework, the GP represents a region located at the boundary between the northern and southern Adriatic subplates. The GP represents the most elevated part of the Apulian foreland, with maximum height around 1000 m, and is structured in an elongated anticline affected by faults trending NW-SE, *E*-W and subordinately NE-SW (Argnani et al., 2009). The nature and development sequence of the GP fault system is still a matter of debate. Some studies highlight the role of strike-slip motion along E-W major faults, e.g. the Mattinata and Rignano faults (Brankman and Aydin, 2004). Other studies emphasise the contribution of compressive deformation related to the stress field from the Dinarides, with direction N-S and NE-SW (e.g. Bertotti et al., 1999). The most recent sediments occurring in the GP are shallow water marine deposits of late Miocene age, exposed today at 100 m height above sea level. Therefore, the onset of uplift in the region might have started during late Miocene to Pliocene, with a minimum estimated uplift rate 0.1 mm/yr (Bertotti et al., 1999, and references therein).

Two superimposed extensional phases can be observed in the GP. The first one is characterized by NE-SW extension, probably occurring during late Cretaceous (Winter and Tapponnier, 1991), whereas the second was directed NW-SE during Paleogene (Argnani et al., 2009). Extension precedes a phase of compression during late Miocene-Pliocene, both onshore and offshore (Bertotti et al., 1999; Brankman and Aydin, 2004). The compressive phase is coupled with thrusting along NW-trending, SW-verging high angle faults, and inversion of pre-existing normal faults (Bertotti et al., 1999; Brankman and Aydin, 2004). This is a common trend in the southern Mesozoic Tethyan margin in Apulia and North Africa (e.g. Roure et al., 2004; Scrocca et al., 2007; Roure et al., 2012), where the increase in hinterland/foreland coupling led to the reactivation of older structures in the lower plate (Roure et al., 2012, and references therein). Contractional deformation can also be traced in the central Adriatic domain, in proximity of the GP, where a thin-skinned tectonic phase superimposes the older Cretaceous and Tertiary inversions of normal faults (Scrocca et al., 2007).

At present day, low to moderate seismicity is recorded in Apulia. On

the other hand, the GP historical seismicity is much more intense, with about 15 earthquakes characterized by $M_W > 5.5$ since 1361 (Rovida et al., 2019). The hypocentral depths and other features of the largest earthquakes in the region show that the present-day stress field affecting the basement of the GP is mostly compressional. In addition, clusters of shallow extensional earthquakes have been recently detected SW of the promontory (Heidbach et al., 2019; Filippucci et al., 2020; Miccolis et al., 2021).

The GP was affected by anorogenic magmatism during Paleocene. This magmatic phase did not only occur in the GP, but is rather widespread throughout the Mediterranean and surrounding regions and is commonly referred as the Circum-Mediterranean Anorogenic Cenozoic Igneous (CiMACI) province (Lustrino and Wilson, 2007, and references therein). Gravimetric studies detected positive anomalies in the entire Apulian area (Tassis et al., 2013), which have been interpreted as resulting from the emplacement of mafic igneous bodies at various depths in the crust (Loddo et al., 1996). The GP igneous bodies crop out in Punta delle Pietre Nere (Fig. 1A), intruding upper Triassic sedimentary successions, and consist of amphibole-bearing alkali-gabbros and alkali-syenite rocks of age 58 and 62 Ma respectively, with lamprophyric affinity (Mazzeo et al., 2018, and references therein). The gabbroic body contains subordinated pyroxenite and is interpreted as part of a more extensive layered intrusion (De Fino et al., 1981).

Due to major compositional differences (Mazzeo et al., 2018) and the long time span between the emplacement of gabbros and alkali-syenites (Bigazzi et al., 1996), it is unlikely that there is a genetic link between the two igneous bodies. These rocks show geochemical affinity with ocean island basalts series and an intermediate composition between depleted mantle material, enriched material and Hi-μ sources, with particularly pronounced latter one. A recent study (Mazzeo et al., 2018) suggests that these rocks might derive from partial melting of an amphibole-rich lithospheric mantle at depths exceeding 70–90 km and pressure of 2.5–3.5 GPa, corresponding to the spinel-garnet transition depth. The geodynamic conditions leading to partial melting are still a matter of debate. However, there exists a general consensus on mantle plume components characterizing these rocks (e.g. Lustrino and Wilson, 2007). Given the small volume and short duration of magmatic activity in the GP, a mantle diapir impinging the area may have small size and/or low potential temperature, making its detection difficult (e.g. Kuritani et al., 2017; Koptev et al., 2021).

These factors have been taken into account in the heterogeneous stress field and in the lithological composition adopted in our numerical simulations.

3. The model

The investigated crustal section has a length of 60 km and width of 32 km (Fig. 2) with SW-NE orientation following the A-B lineament (Fig. 1B). The seismicity distribution follows a vertical trend SW of the GP and a deep sub-horizontal distribution toward NE.

We test the hypothesis that seismicity in the GP can be related not only to the interactions between lithology and stress conditions in the region, but also to fracturing and fluid presence. Therefore, we include in the model the presence of zones where fracking and fluids occur (light blue zones in Fig. 2), taking into account their effect on rock thermal and rheological parameters (pore fluid factor λ, cohesion factor S, thermal conductivity k_i, Table 1). The size and shape of these zones are based on hypocenter locations in the GP (Fig. 1). The crustal section consists of 6-layers, each characterized by different lithologies and corresponding different thermal and mechanical parameters. Thickness and petrological parameters of each layer correspond to crustal characteristics of the Adria plate and, where possible, to the constraints from geophysical data for the GP. The 3 top layers represent the sedimentary cover of the Adria crust, whereas the 3 layers underneath represent the crystalline basement. The sedimentary cover overlays a Hercynian basement that has been documented for the Apulian margin in a number of previous studies (e.g. Schenk, 1981). Further information on the petrological characteristics of the GP crust is available in Appendix A, while minerals percentage for each layer and corresponding rheological parameters are specified in Table 2. The lithologies constituting the crustal layers are given in Amato et al. (2014) and Morsili (2016) while the relative parameters are given in Table 1.

We construct a steady-state 2D thermal model providing the temperature field and surface heat flow in a multilayered crust (see Fig. 2 for details). The temperature $T(x,z)$ is calculated, taking into account the characteristics of each i-th layer, by the steady state heat equation:

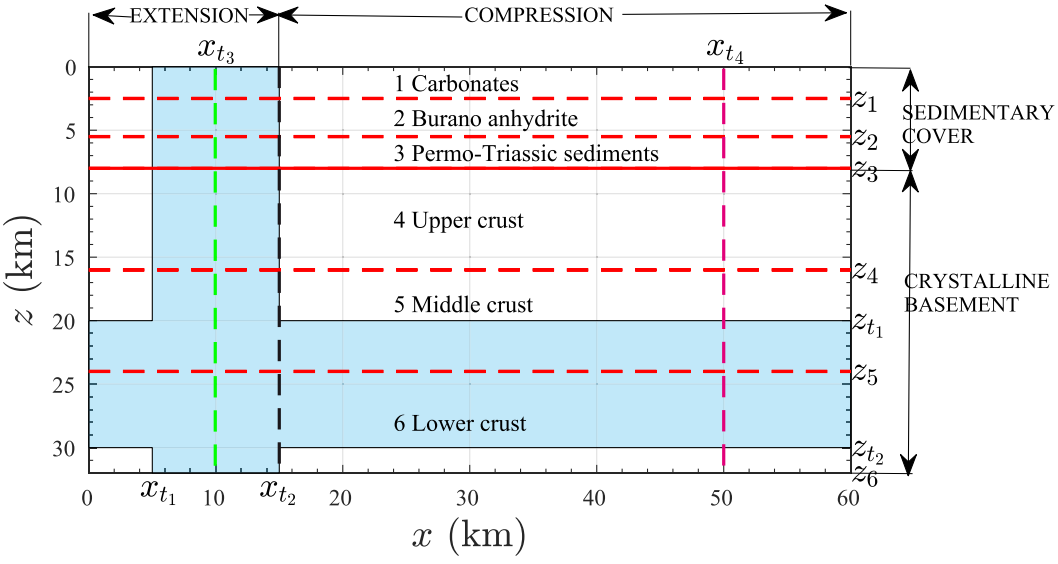

Fig. 2. Sketch of the model. Horizontal lines: the dashed red lines indicate the i-th layers boundary ($z = z_i$), the solid red line indicates the boundary between the sedimentary cover and the crystalline basement ($z = z_3$). Vertical lines: the green ($x = x_{t3}$) and magenta ($x = x_{t4}$) dashed lines indicate the two vertical profiles where significant model results are calculated, the black dashed line ($x = x_{t2}$) indicates the boundary between extensional and compressional tectonic regime. The light blue area is affected by the presence of fluids, fracturing or both. (For interpretation of the references to color in this figure legend, the reader is referred to the web version of this article.)

Table 1
Parameters of the model. A) independent on layer, B) dependent on layer. (*Amato et al. (2014); **Carmichael (2017); †Clauser and Huenges (1995); ††Gerya (2009); ‡ Ranalli (1995); ‡ ‡Smith and Faulkner (2010) and references therein).

A

Parameter	Symbol	Value	U.m.
Surface temperature ($z = 0$)	T_0	20	°C
Base temperature ($z = z_6$) (Geotherm I and II)	T_b	500	°C
Base temperature ($z = z_6$) (Geotherm III and IV)	T_b	450	°C
Surface Radiogenic heat production ($z = 0$)	H_0	2	μW m^{-3}
Acceleration of gravity	g	9.8	m s^{-2}
Characteristic depth	D	12	km
Gas constant	R	8.314	J K^{-1}mol^{-1}
Thermal expansion coefficient††	α	$5 \cdot 10^{-6}$	K^{-1}
Friction coefficient‡‡	κ	0.5	–
Strain rate‡	$\dot{\varepsilon}$	10^{-14}	s^{-1}
Solver minimal residual	ζ	10^{-6}	–
Cohesion factor** (fractured; unfractured)	S_f; S_u	10; 75	MPa
Pore fluid factor** (dry; wet)	λ_d; λ_w	0.4; 0.8	–

B

Parameter	Symbol	Layer i						U.m.
		1	2	3	4	5	6	
Layer depth bottom	z_i	2.5*	5.5*	8	16	24	32	km
Layer thickness	th_i	5.5*	3*	2.5	8	8	8	km
Layer depth bottom (case D)	z_i	2.5*	5.5*	8	14	20	32	km
Layer thickness (case D)	th_i	5.5*	3*	2.5	6	6	12	km
Surface density**	ρ_{0i}	2450	2250	2500	2750	2800	2900	kg m^{-3}
Specific heat at c. p.	C_{pi}	800	800	800	1000	1000	1000	J K^{-1} kg^{-1}
Conductivity† (dry)	k_{di}	2.1	2.0	2.5	2.7	2.5	2.4	W K^{-1} m^{-1}

Table 2
A) Parameters adopted for each case. Bold characters indicate variations in parameters with respect to the preceding case. B) Mineral assemblage and resulting rheological parameters for each layer. A_i, n_i and Q_i values relative to single minerals are given in Lavecchia et al. (2016) and references therein. See text for the description of the methodology adopted to calculate A_i, n_i, and Q_i. Cc = calcite, Qtz = quartz, Dm = dolomite, Mc = phyllosilicates, Ab = albite, Als = aluminosilicates, An = anorthite, Px = pyroxene, Ol = olivine, Grt = garnet.

A

Parameter		Symbol	Cases							U.m.
			A	B	C	D	E	F	G	
Geotherm			I	I	**II**	**III**	**IV**	IV	IV	
Depth bottom of layer 4		z_4	16	16	16	**14**	**16**	16	16	km
Depth bottom of layer 5		z_5	24	24	24	**20**	**24**	24	24	km
Base temperature		T_b	500	500	500	**450**	450	450	450	°C
Cohesion factor	Unfractured	S_u	75	75	75	75	75	75	75	MPa
	Fractured	S_f	–	**10**	10	10	10	10	10	
Pore fluid factor	Dry	λ_d	0.4	0.4	0.4	0.4	0.4	0.4	0.4	–
	Wet	λ_w	–	–	**0.8**	0.8	0.8	0.8	0.8	
Presence of mafic rocks			No	No	No	No	No	**Yes**	Yes	
Sedimentary protholith in layer 5			No	No	No	No	No	No	**Yes**	

B

Layer	Composition	A_i	n_i	Q_i
i	% vol	MPa^{-n}s^{-1}	–	kJ mol^{-1}
1	Cc65, Qtz10, Dm25	$2.4 \cdot 10^{-1}$	3.28	182
2	Qtz20, Dm80	$3.3 \cdot 10^{-6}$	3.18	161
3	Cc10, Mc30, Qtz30, Dm10, Ab20	$1.7 \cdot 10^{-6}$	6.23	163
4	Cc5, Mc35, Qtz35, Ab15, Als5, An5	$6.9 \cdot 10^{-8}$	7.15	173
5	Mc15, Qtz30, Ab35, An20	$3.4 \cdot 10^{-6}$	5.00	204
5 (case F)	Mc10, Qtz20, Ab23, An23, Px20, Ol4	$1.2 \cdot 10^{-10}$	4.26	236
5 (case G)	Mc24, Qtz19, Ab21, An9, Px23, Ol4	$2.7 \cdot 10^{-5}$	5.37	212
6	Mc12, Qtz25, Ab25, Als7, Grt14, Px14, Ol3	$2.8 \cdot 10^{-4}$	4.70	269
6 (case F)	Mc8, Qtz17, Ab16, Als5, Grt9, Px29, Ol5	$1.9 \cdot 10^{-3}$	4.10	269

$$\nabla\cdot\left(\frac{k_i}{\rho C_{pi}}\nabla T\right) = H \tag{1}$$

where k_i is the thermal conductivity for each i-th layer and is equal to k_{di} or $k_{wi} = 3k_{di}$ depending on fluid-unsaturated or saturated condition respectively (Clauser and Huenges, 1995, and references therein), ρ is the density, C_{pi} is the specific heat at constant pressure and H is the radiogenic heat production, given by:

$$H(z) = H_0 exp\left(-\frac{z}{D}\right) \tag{2}$$

where H_0 is the radiogenic heat production at the Earth's surface, D is the characteristic depth and z is the depth. The density $\rho(x,z)$ is temperature-dependent, according to the equation:

$$\rho(x,z) = \rho_{0i}\{1-\alpha[T(x,z)-T_0]\} \tag{3}$$

where ρ_{0i} is the density of rocks at surface temperature and pressure and α is the thermal expansion coefficient for crustal rocks. $T(x,z)$ is calculated with the boundary conditions $T(x,0) = T_0$ at the surface and $T(x, z_6) = T_b$ at the base. Temperature at the base of continental crust shows a wide range of variations (e.g. Pasquale et al., 1990; Schutt et al., 2018; Gruber et al., 2021). Two values of T_b (450 and 500 °C) have been adopted to test the sensitivity of the models to base temperatures. These values are chosen to best fit the calculated heat flow at surface with the surface heat flow values measured in the GP region (Della Vedova et al., 2001).

We numerically solved Eq. (1) by using FreeFEM++ (Hecht, 2012) a software specifically designed to solve systems of partial differential equations (PDEs). This software is based on the finite element method to solve linear and nonlinear multi-equation systems in an automated framework, and provides mesh generators and easy geometric input. The mesh adopted for the model is composed of triangular elements and it is based on the Delaunay-Voronoi algorithm. This ensures the minimization of sliver triangles in the model domain, and therefore improves the accuracy and speed of the PDEs solver. Several element sizes have been tested to obtain an accurate solution and a fast calculation speed. We have verified that a valid choice is represented by a mesh built from elements with edges of 250 m around the domain boundaries. Therefore, this size has been adopted for all simulations. The solver implemented is the generalized minimal residual method, with an imposed minimal residual $\zeta = 10^{-6}$.

The heat flow $\mathbf{q}(x,z)$ is computed by:

$$\mathbf{q}(x,z) = k_i \nabla T(x,z) \tag{4}$$

and its surface vertical component $q_0(x,0)$ is compared with the surface heat flow map (Della Vedova et al., 2001) along the A-B lineament (Fig. 1B) in order to validate the geothermal model.

We adopt a rheological model to evaluate the brittle-ductile behavior of the crustal section. The differential shear stress $\Delta\sigma_m(x,z)$ for faulting, which is the fault strength, is calculated by adopting the Coulomb-Navier criterion (Yin and Ranalli, 1992):

$$\Delta\sigma_m(x,z) = \frac{2\kappa\rho g z(1-\lambda)+2S}{(\kappa^2+1)^{\frac{1}{2}}\pm\kappa} \tag{5}$$

where κ is the coefficient of steady sliding friction, g is the acceleration of gravity, λ is the pore fluid coefficient and corresponds to λ_d or λ_w depending on hydrostatic or near-lithostatic conditions respectively, S is the cohesion coefficient and corresponds to S_u or S_f depending on unfractured or fractured conditions respectively. The values of S and λ (Table 2) are independent on lithology and vary in proximity of the simulated seismogenic structures (Fig. 2). We take into account the drop of $\Delta\sigma_m$ due to fractures through the coefficient S and due to fluid presence through the coefficient λ. Several values of λ have been tested to determine when pore fluid pressure is high enough to cause a switch in the rheology of the lower crust, from hydrostatic (λ=0.4) to near-lithostatic (λ=0.8) values. Fracturing and faulting can induce porosity and subsequently determine a loss of cohesion, favoring a brittle regime. The stress field pattern (Miccolis et al., 2021) shows a compressive regime for the NE part of the GP, whereas evidence of an extensive regime exists for the SW part of the GP (Filippucci et al., 2020). The deformation regime exerts a primary control over rock strength in geodynamically active regions (e.g. Neely and Stein, 2021). Therefore, compressional/extensional deformation is modeled by introducing a $\pm$ operator in Eq. (5) (+ for extension, − for compression).

Under the assumption of power-law creep, the maximum tectonic differential shear stress $\Delta\sigma_M(x,z)$ is calculated by adopting the Dorn equation (Gerya, 2009; Filippucci et al., 2019b):

$$\Delta\sigma_M(x,z) = \left(\frac{\dot{\varepsilon}}{A_i}\right)^{\frac{1}{n_i}} exp\left(\frac{Q_i}{n_i RT}\right) \tag{6}$$

where $\dot{\varepsilon}$ is the strain rate, n_i is the exponent of the rheological power-law creep, A_i is the Dorn parameter, Q_i is the activation energy, R is the gas constant and T is the absolute temperature. Each lithology is polymineralic and each mineral composing the crust layers has distinct values of rheological parameters. Therefore, the parameters of minerals and their volume percentage are used to calculate A_i, n_i and Q_i for each layer. The details of the averaging method are fully described in Ji et al. (2003). The strain rate $\dot{\varepsilon} = 10^{-14}$ s^{-1} is an average value for geodynamically active areas (e.g. Ranalli, 1995; Fagereng and Biggs, 2019).

The rheological behavior of the crust can be defined by the minimum differential stress

$$\sigma_d(x,z) = min[\Delta\sigma_M(x,z)\,;\Delta\sigma_m(x,z)] \tag{7}$$

representing the crustal strength. For $\sigma_d(x,z) = \Delta\sigma_M(x,z)$ the rheological behavior is brittle; while for $\sigma_d(x,z) = \Delta\sigma_m(x,z)$ the rheological behavior is ductile. As a consequence the crustal rheology can be represented by the step function

$$Rh(xz) = \begin{cases} 0, & \text{if} \quad \sigma_d = \Delta\sigma_M(x\,z) \\ 1, & \text{if} \quad \sigma_d = \Delta\sigma_m(x\,z) \end{cases} \tag{8}$$

4. Results

The parameters adopted in each simulation case are summarized in Table 2A. In our simulations the crust is composed of layers with thickness th_i and bottom depth z_i. The layer thickness is kept constant in all the simulations, except for the case D (Table 2A). In order to evaluate the effect of parameters on rheology we adopt four different geotherms, assuming two different values of T_b and pore fluid pressure at either hydrostatic or near-lithostatic conditions in correspondence of low cohesion zones (light blue area of Fig. 2). For each geotherm we test the effect of variations in cohesion factor S, pore fluid factor λ, thickness of the crystalline basement layers (th_4, th_5, th_6) and petrological composition on σ_d and Rh. A flow chart in Appendix B (Fig. B.1) summarizes the procedure followed for the model development and the obtained results. The results of the model are shown in Figs. 3–6 and Appendix C.

4.1. Crustal strength σ_d

When rocks are subjected to compression, the maximum value of σ_d in the sedimentary cover is constant independent of the investigated

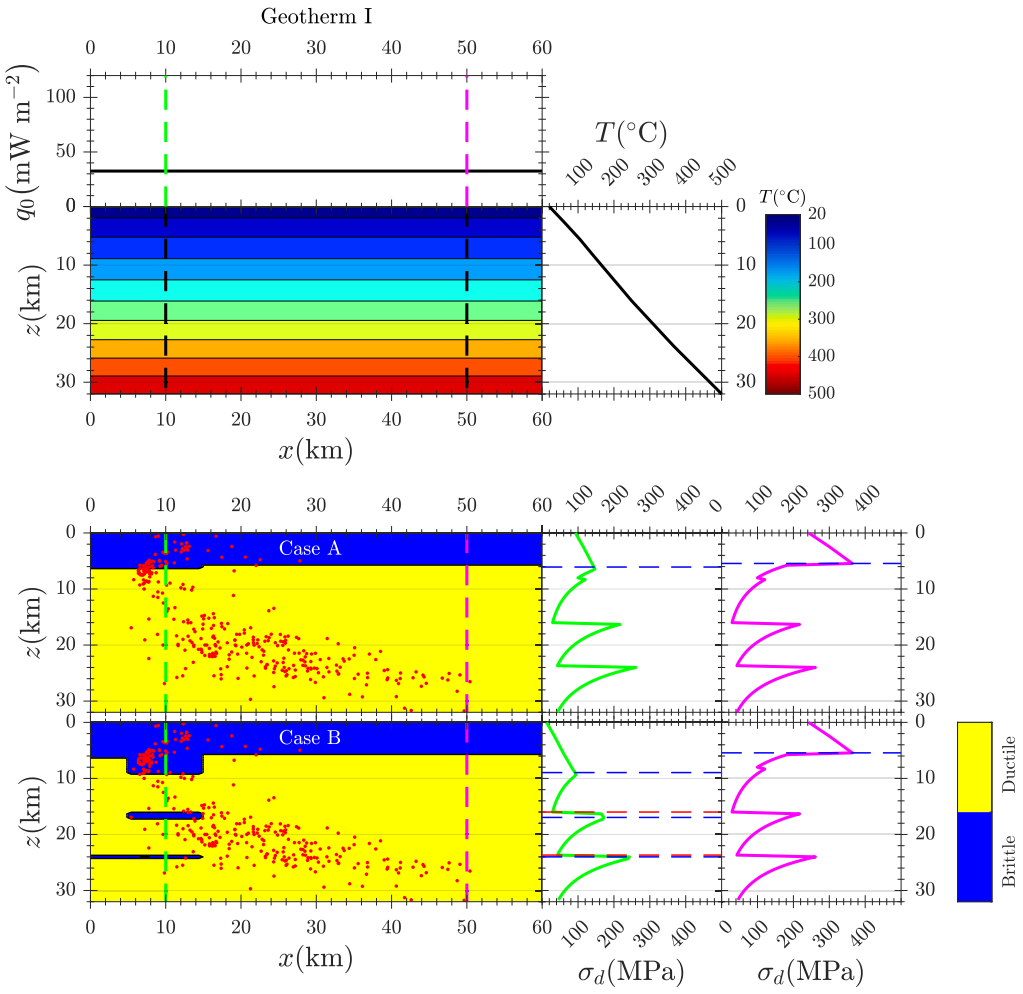

Fig. 3. Geotherm I and Cases A and B. Upper panel: 2D Temperature $T(x,z)$, surface heat flow $q_0(x)$, temperature $T(z)$ along the black vertical dashed lines. T_b = 500°C. Lower panels: rheological structure $Rh(x,z)$, differential stress $\sigma_d(z)$ with colours referring to the vertical dashed lines. Horizontal dashed lines refer to the brittle-to-ductile boundary (color blue) and to the ductile-to-brittle boundary (color red) for increasing depth. Case A: dry unfractured condition, Case B: dry fractured condition in the light blue area of Fig. 2. The parameters adopted to plot the graphs are shown in Tables 1, 2. (For interpretation of the references to color in this figure legend, the reader is referred to the web version of this article.)

setting, with $\sigma_d \approx 360$ MPa. Differently, in the same layer σ_d is significantly lower when extension occurs and is subjected to large variations. In unfractured conditions (case A), $\sigma_d \approx 150$ MPa, whereas $\sigma_d \approx 60$ MPa in regions with low cohesion (case B) and $\sigma_d \approx 20$ MPa in near-lithostatic conditions (cases C-G). The strength σ_d calculated in the crystalline basement is significantly lower than in the sedimentary cover in compressive areas. In the basement, the calculated maximum value of σ_d is less than 260 MPa (cases A and B) and further decreases to 140 MPa when fluids are present in the lower crust (case C). A rise in σ_d takes place when a colder geotherm is adopted (cases D-G). It results in σ_d between 160 MPa when either a granodiorite or metasedimentary middle crust is implemented (cases E and G), and 220 MPa when we investigate a thicker lower crust (case D). One exception is when mafic rocks are present in the basement (case F). In this simulation, the change of basement composition, and in particular the presence of pyroxene and olivine, lead to values of σ_d of approximately 500 MPa in a thin layer at the top of the injected middle crust.

4.2. Crustal rheology Rh

All simulations show a brittle behavior for most of the sedimentary cover in both compressional and extensional settings. The brittle-ductile transition is located at a depth of 6 km and its depth variations, due to changes in the geotherm and compressional-to-extensional setup, are negligible. The crystalline basement retains a ductile behavior in the absence of fluids, regardless of the adopted geotherm. This can be promptly observed in unfractured, dry conditions (case A). Low values of cohesion (case B) in the extensional domain can lead to a deepening of the brittle-ductile transition to a depth of 10 km and the appearance of thin brittle layers deeper in the crystalline basement. However, the domain subjected to compression is totally unaffected by low cohesion.

The presence of fluids exerts a more profound effect on the crustal rheology and can cause a change to thick brittle layers in the previously ductile crystalline basement. In the lower crust, fluids cause an increase in thermal conductivity and, therefore, variations in geotherm (case C). This is combined with high values of the pore fluid factor and causes well-developed brittle regions where the crust is subjected to extension. In contrast, where compression occurs and $T_b = 500$°C, the crust is only slightly affected by fluids. Consequently, the ductile behavior is still retained, except for very high values of $\lambda = 0.8$. In this scenario,a thin brittle layer marks the boundary between middle and lower crust. In order to test the sensitivity of the model to different geotherms, a colder temperature field has been implemented, based on a temperature at the bottom of the crust $T_b = 450$°C (geotherm III and IV, cases D-G). In the resulting simulations the combined effect of high thermal conductivity, high pore fluid factor, low cohesion and low temperatures causes thick brittle layers in the extensional domain of the model (case D). These layers affect both the middle and the lower crust, with depths between 20 km and 30 km. On the other hand, where compression occurs only the lower crust shows a brittle behavior in a 4 km thick layer, whereas the middle crust rheology remains unaffected by fluid presence. The brittle region within the crystalline basement is well defined, but still too thin to be compatible with the presence of the seismogenic layer at the base of the GP crust. Therefore, we tested the sensitivity of this region's thickness to variations in crustal composition and lower crust thickness. When the lower crust extends from a depth of 20 km down to the base of

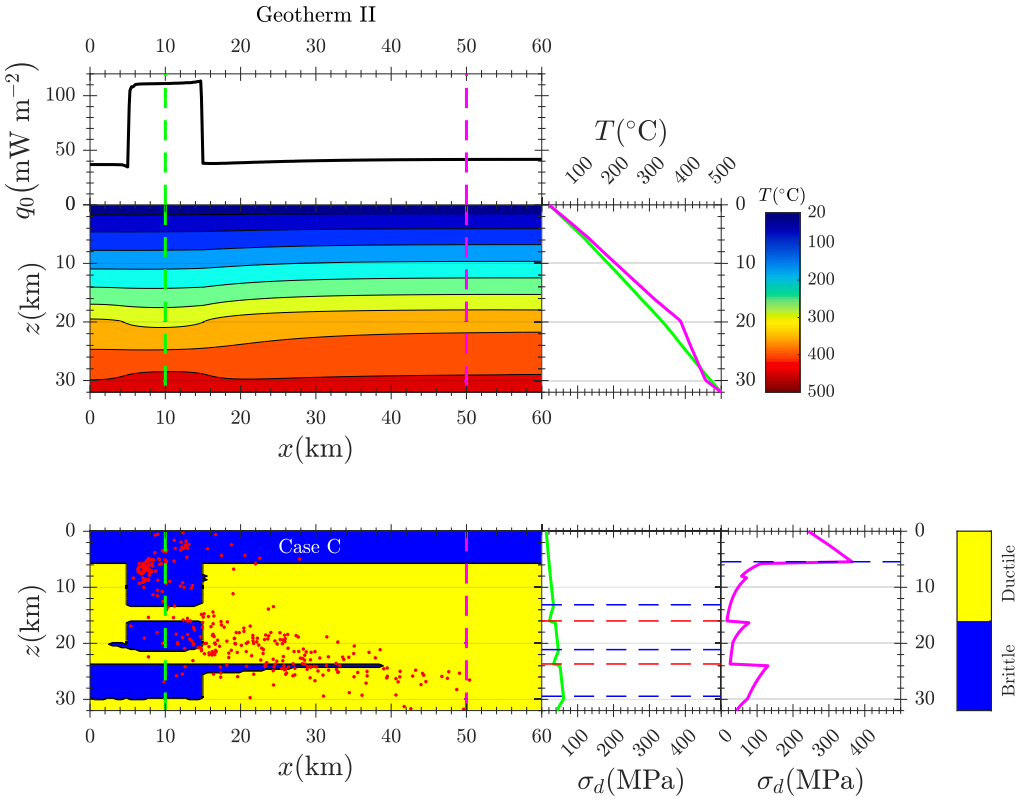

Fig. 4. Geotherm II and Case C. Upper panel: 2D Temperature $T(x,z)$, surface heat flow $q_0(x)$, temperature $T(z)$ with colours referring to the vertical dashed lines. T_b = 500°C. Lower panels: rheological structure $Rh(x,z)$, differential stress $\sigma_d(z)$ with colours referring to the vertical dashed lines. Horizontal dashed lines refer to the brittle-to-ductile boundary (color blue) and to the ductile-to-brittle boundary (color red) for increasing depth. Case C: wet and fractured condition in the light blu area of Fig. 2. The parameters adopted to plot the graphs are shown in Tables 1, 2. (For interpretation of the references to color in this figure legend, the reader is referred to the web version of this article.)

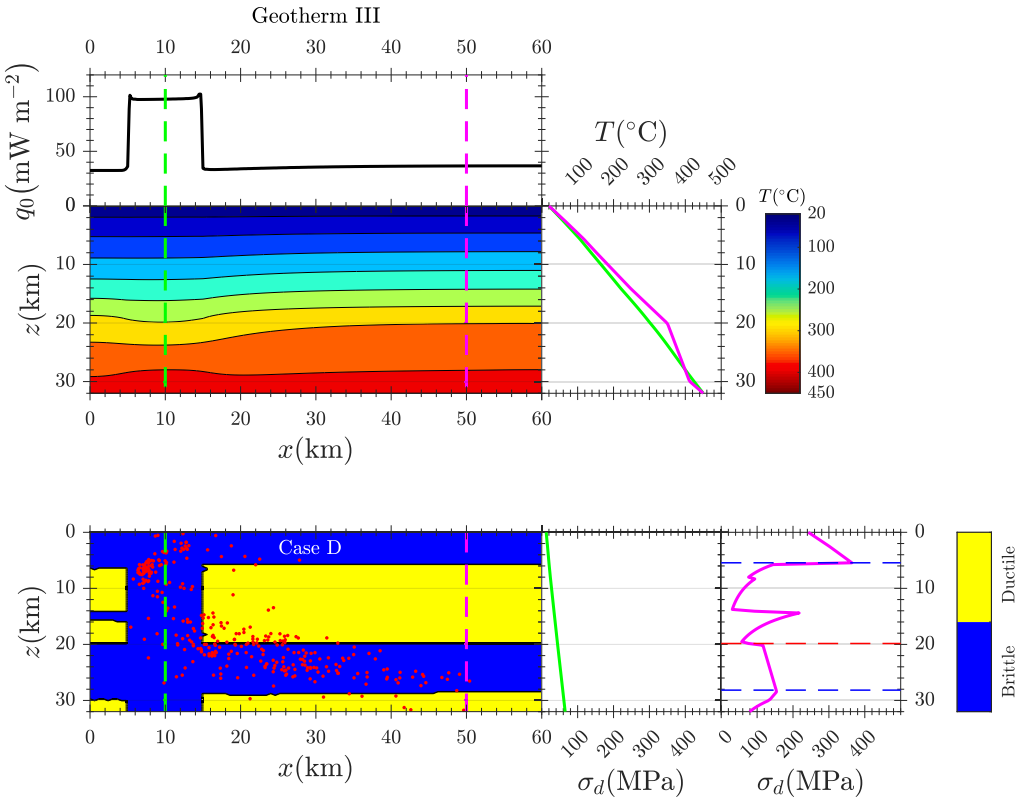

Fig. 5. Geotherm III and Case D. Upper panel: 2D Temperature $T(x,z)$, surface heat flow $q_0(x)$, temperature $T(z)$ with colours referring to the vertical dashed lines. T_b = 450°C. Lower panels: rheological structure $Rh(x,z)$, differential stress $\sigma_d(z)$ with colours referring to the vertical dashed lines. Horizontal dashed lines refer to the brittle-to-ductile boundary (color blue) and to the ductile-to-brittle boundary (color red) for increasing depth. Case D: wet and fractured condition in the light blue area of Fig. 2, lower crust thicker. The parameters adopted to plot the graphs are shown in Tables 1, 2. (For interpretation of the references to color in this figure legend, the reader is referred to the web version of this article.)

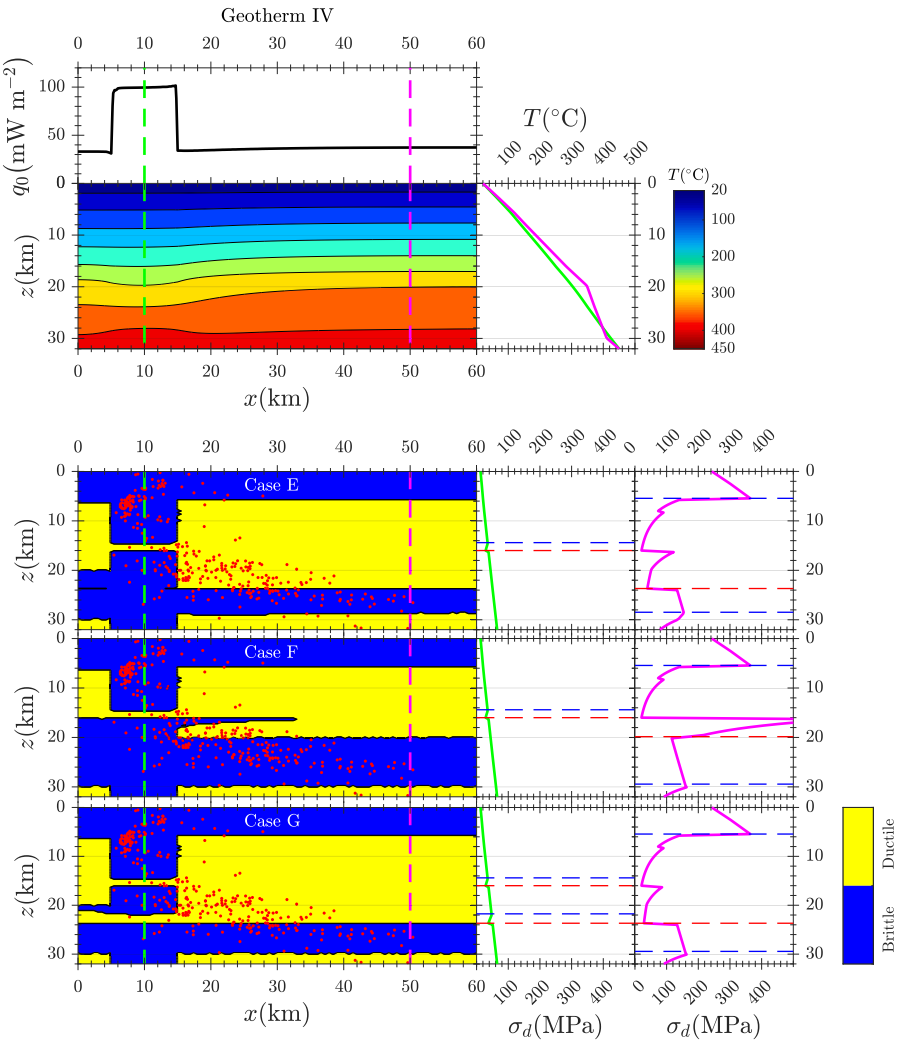

Fig. 6. Geotherm IV and Cases E, F, G. Upper panel: 2D Temperature $T(x,z)$, surface heat flow $q_0(x)$, temperature $T(z)$ with colours referring to the vertical dashed lines. T_b = 450°C. Lower panels: rheological structure $Rh(x,z)$, differential stress $\sigma_d(z)$ with colours referring to the vertical dashed lines. Horizontal dashed lines refer to the brittle-to-ductile boundary (color blue) and to the ductile-to-brittle boundary (color red) for increasing depth. For all cases: wet and fractured condition in the light blue area of Fig. 2. Case F: Gabbros. Case G: Gabbros+metasediment. The parameters adopted to plot the graphs are shown in Tables 1, 2. (For interpretation of the references to color in this figure legend, the reader is referred to the web version of this article.)

the model, it overlaps the region of fluid presence (case C). As a result, the brittle layer has a thickness of 8–10 km, with its upper boundary coinciding with the middle-lower crust boundary. The presence of mafic rocks in the GP has been taken into consideration by carrying out simulations where they constitute part of the crystalline basement, up to 35% vol (cases F and G). There is a high degree of uncertainty on the characteristics of the mafic rocks intruding the Apulian basement. However, reflective magmatic bodies have been detected at mid-crustal depth in previous seismic studies (Finetti and Del Ben, 2005), while a thick band of parallel reflectors has been detected in the lower crust and interpreted as layering (Amato et al., 2014). For these reasons, the mafic component has been added at middle and lower crust depth. In addition, simulations where mafic rocks are also present in the upper crust and in variable %vol are included in Appendix C (Fig. C.1). All these simulations are characterized by a significant increase in rock strength, with values exceeding 500 MPa in the middle crust (case F). Moreover, brittle behavior is no longer confined within the lower crust, but now it also affects the middle crust, in both the compressional and extensional domains, in a similar fashion to the layered,"corset-like" model proposed by Meissner and Kern (2008). As a consequence, the simulated brittle layer can exceed a thickness of 10 km. On the other hand, a metasedimentary middle crust composition (case G) still retains a ductile rheology, even if partly constituted by mafic rocks. Therefore, in this simulation the brittle layer is significantly thinner than the preceding cases and does not exceed a thickness of 6 km. Further simulations have been carried out to test the sensitivity of rheology variations to fluid presence and strain rate (Fig. C.1 in Appendix C). These additional simulations confirm the pivotal role of fluids to promote a brittle rheological behavior at depth in the crust, even when mafic rocks are present in the entire crystalline basement or the deformation rate is very high.

We tested the effect of variations in S and λ on σ_d where the crystalline basement is partly composed of mafic rocks for a percentage of 35%vol, and for geotherms calculated on the basis of a temperature at the base of the model of 500˚C (Fig. C.2 a, c and e) and 450˚C (Fig. C.2 b, d and f). In areas where extension occurs, (Fig. C.2 a and b), a decrease in S is enough to generate drops in σ_d and rheological variations from ductile to brittle behavior, regardless of the adopted geotherm. In contrast, regions where compression occurs retain a ductile behavior regardless of the cohesion value or geotherm adopted. An increase in λ leads to a further expansion of the ductile field in regions of the model subjected to extension (Fig. C.2 c and d). Where compression occurs, the effect of λ increase is almost negligible when the adopted temperature at the base of the model is 500˚C (Fig. C.2 e). When λ is very high and for lower temperatures, a switch of rheological behavior from ductile to brittle occurs (Fig. C.2 f).

4.3. Effects of geotherms on surface heat flow q_0

Fluid presence has a significant effect on the thermal state of the crust. Therefore, by influencing the values of thermal conductivity of rocks, fluids also affect the heat flow in the crust. In areas where water is not present, we calculate a value of surface heat flow $q_0 \approx 30\,\mathrm{mW\ m^{-2}}$ (geotherm I). Differently, the presence of fluids at the bottom of the model leads to higher thermal conductivity and higher temperatures in the fluid rich layer (geotherm II). This is accompanied by a value of surface heat flow $q_0 \approx 40\,\mathrm{mW\ m^{-2}}$. When a region rich in fluids covers the whole crustal thickness, the increase in thermal conductivity is significant enough to determine a large rise in surface heat flow, with $q_0 \approx 110\ \mathrm{mW\ m^{-2}}$ when $T_b = 500$˚C (geotherm II), and $q_0 \approx 100\ \mathrm{mW\ m^{-2}}$ when $T_b = 450$˚C (geotherms III and IV). This effect is partly mitigated by lower values of thermal gradient, especially where the horizontal and vertical fluid-rich intervals intersect.

5. Discussion

We investigated the effect of fluid presence, thermal state, lithology, fractures and heterogeneous tectonic stress regime on crustal rheological properties in the GP, comparing our results with the recorded seismicity distribution and surface heat flow measured in the area (see for details the workflow in Appendix B, Fig. B.1). Our results are illustrated in Fig. 8. With this study we provide a rheological model that highlights the main mechanisms generating: 1) the presence of layers within the GP lower crust where earthquakes can potentially nucleate, and 2) the marked heat flow anomaly in the area SW of the GP.

Rheological models, obtained by using geotherms III and IV, which reproduce the observed surface heat flow, are able to explain brittle deformation not only in the domain SW of the GP but also in the NE (Figs. 5 case D, 6 case F) and show some differences among them. It appears that the main parameters affecting the rheological behavior of the crust are the water presence (k_i and λ) and the temperature at the base of the crust T_b. The petrological composition and layer thickness variations affect the thickness of the brittle layer in the lower crust, improving the match with the observed deep seismicity (Figs. 5 case D, 6 case F).

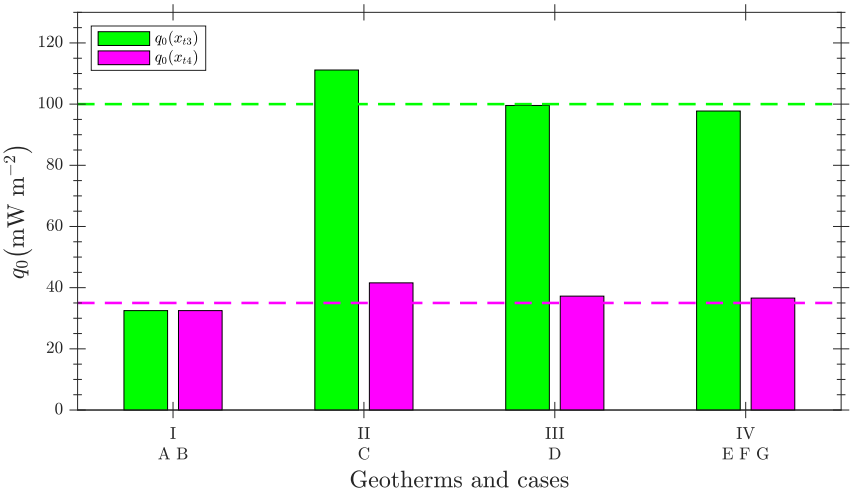

Fig. 7. Comparison between surface vertical heat flow $q_0(x_{t3})$ and $q_0(x_{t4})$ calculated by the model (bars) and reported in Della Vedova et al. (2001) (dashed lines). The green and magenta colours refer to the points $x = x_{t3}$ and $x = x_{t4}$ shown in Fig. 2 respectively. Case D represents the best agreement between calculated and measured values of q_0. (For interpretation of the references to color in this figure legend, the reader is referred to the web version of this article.)

5.1. Rheology of the GP: Implications for seismicity and surface heat flow

As pointed out above the new seismic data acquired by the GSN (Fig. 1A) show that the seismicity of the GP can be subdivided into two main clusters. A first cluster is located in the area SW of the GP and is characterized by a microseismicity involving the whole crust down to a depth of 20 km (Miccolis et al., 2021) and surface heat flow $q_0 \approx 100$ mW m^{-2} (Della Vedova et al., 2001). A second cluster involves the whole GP, and is characterized by deep microseismicity in the middle-lower crust (Miccolis et al., 2021), slightly more intense than the activity observed SW of GP, and surface heat flow $q_0 \approx 40$ mW m^{-2} (Della Vedova et al., 2001) with foci distributed along a layer gently dipping NE, at depth between 20 and 30 km (Miccolis et al., 2021).

Cases A and B do not match with the observed surface heat flow and do not produce the expected brittle layer in the lower crust NE of the GP (Figs. 3, 7). Nevertheless, these cases are useful to better understand the role of the model parameters. In case A, brittle behavior is confined within the sedimentary cover only, at depth shallower than 7–8 km. Case B shows that, in presence of rock fracturing, a decrease in cohesion factor S triggers an expansion of the brittle field down to upper crustal depths and in the middle and lower crust a ductile behavior is retained even for fractured condition $S = S_f$, which is incompatible with the deep seismic activity in the GP.

A comparison between the calculated surface heat flow and the values reported in Della Vedova et al. (2001) is shown in Fig. 7. For the cases A and B $q_0(x) = 33$ mW m^{-2}. This value is comparable with heat flow data in the GP, but values in the region SW of the GP are much higher. The high surface heat flow measured in this area could be possibly explained by 1) a heat source at depth, such as melts injected in the crust, and 2) a water circulation system transporting heat at a shallower depth and increasing thermal conductivity in a water-rock phase system. Although the presence of magmatic bodies has been detected both buried (e.g. Loddo et al., 1996) and outcropping in Apulia (e.g. De Fino et al., 1981; Lustrino and Wilson, 2007, and reference therein), there is no recorded magmatic activity younger than 58 Ma in the region. In addition, the presence of buried hot magmatic bodies would increase temperature and favour ductile behavior in host rocks. Therefore, the presence of a shallow water circulation system appears to be a more suitable explanation for both the seismic activity and the high heat flow near the Candelaro and Apricena faults.

A pivotal role of the interaction between fluids and temperature is shown in cases C-G, where the pore fluid pressure in the middle/lower crust is in near-lithostatic conditions and therefore $S = S_f$, $k = k_w$ and $\lambda = \lambda_w$. In case C, the lower crust shows brittle behavior in the extensional zone ($x < x_{t2}$), with a ductile behavior almost entirely in the compressional zone. However, the seismically active region in the lower crust has a thickness of around 20 km, presumably overlapping the lower and middle crust. In simulations where the upper, middle and lower crust have approximately the same thickness, a granodiorite middle crust composition strongly favors brittle behavior in an extensional zone ($x > x_{t2}$) and when temperature $T_b = 450$°C (geotherm III, case D). A brittle rheology may also occur in a compressional zone when the middle crust is injected with mafic material (case F) or if the lower crust is particularly thick (case D). It should be noted that the presence of gabbroic rocks in the basement investigated in case F is consistent with the gravimetric anomaly observed both regionally and locally (Loddo et al., 1996; Tassis et al., 2013). It is also important to note that brittle behavior is not predicted when the middle crust is composed of metamorphic rocks derived from sedimentary protholiths, even when injected by mafic rocks (case G). Therefore, it appears that the middle crust has a granodiorite composition and that mafic intrusions could be widespread in the crystalline basement at least at a middle crustal depth (case F).

Our model predicts that brittle deformation is dominant in the sedimentary cover and can further expand down to upper crustal depths where rocks have low cohesion, controlling the distribution of earthquakes at shallow depths in both hydrostatic and near-lithostatic conditions. Differently, the middle and lower crust retain a ductile rheology even where the cohesion factor is low ($S = S_f$). The lower crustal composition is dominated by granulite facies metamorphic rocks, which are nominally dry for a wide range of heat flow and heat production conditions (e.g. Jamtveit et al., 2018). Under such conditions, the rheological behavior will be controlled by the strength of the dry mineral assemblage composing the lower crustal rocks, which can exceed 1 GPa (Ranalli and Murphy, 1987). Earthquakes in the lower crust are thus favored for very high strain rate values, so that the stress threshold for brittle behavior is lower than the one for ductile flow and therefore rock deformation occurs by faulting. Alternatively, a seismogenic lower crust may be present when there are factors that significantly decrease the stress threshold for brittle behavior in granulite facies rocks. Jamtveit et al. (2018) proposed a mechanism for seismicity generation in the lower crust, in response to major earthquakes at shallower depths followed by aftershock propagation and structural transformation in the lower crust. A remarkable characteristic of the GP, however, is the absence of earthquakes at depths shallower than 20 km in areas other than SW of the promontory, and a diffused seismicity at greater depth. In addition, our model highlights a predominant ductile behavior of rocks overlying the lower crust up to the sedimentary cover. Based on our results, it appears that an increase in pore fluid pressure λ may constitute a suitable mechanism for rock weakening and subsequent rheology switch from ductile to brittle in the lower crust. High values of λ may occur for a number of reasons, including metamorphic dehydration reaction and volumetric expansion (e.g Gao and Wang, 2017, and references therein) or presence of pressurized cracks below layers of impervious rocks (Zencher et al., 2006). Previous studies also show a relationship between pore pressure, faults and stress tensor orientation (Byrelee, 1992). Lastly, tectonic events, such as tectonic compaction in the foreland and variations in fracture systems characteristics can cause remarkable variations in fluid circulation and pressure (e.g. Roure et al., 2005). In our case, the thick ductile sedimentary cover and basement above the brittle layer suggests low permeability of rocks overlying the fluid-rich lower crust and therefore a stagnation of fluids in mechanical equilibrium with the surrounding rocks. The presence of fluids in the lower crust has been well documented in a number of seismic, magnetotelluric and electric studies (e.g. Simpson, 1999, and references therein) and has been invoked as a trigger for an increase in strain (e.g. Iio et al., 2002) and, potentially, seismicity in many different areas (e.g. Deichmann, 1992; Balfour et al., 2015). This is favored in geodynamic conditions where short-lived, pulsating weakening mechanisms occur (e.g. Noda et al., 2009) and lead to rapid pore fluid pressure variations (Chen and Nur, 1992, and references therein). At the same time, earthquakes in the CF area are less frequent and less energetic than earthquakes occurring in the lower crust of the GP. Therefore, we are inclined to rule out stress transfer from the CF to the lower crust as main trigger for deeper seismic activity in the GP, although its contribution cannot be excluded. Further studies are evidently needed to better assess the stress transfer role in GP earthquake generation.

In presence of shallow fluid, seismic activity should be not confined only to the lower crust, but it should be more evenly distributed across the crust as it happens in the CF. In contrast, in the GP shallow seismic activity does not occur and, therefore another fluid source is necessary to generate the observed seismicity.

5.2. Origin of fluids and dipping of the lower crust seismogenic layer

Our results show that the rheological behavior of the GP crystalline basement largely depends on the presence of fluids at depth. However, a fluid source beneath the promontory has not been unambiguously identified. The GP magmatic phase during Palaeogene times was not only restricted to the small dykes today exposed in Punta delle Pietre Nere. It is part of a much more extended magmatic phase, affecting broad sectors in the Adriatic domain (Improta et al., 2014, and

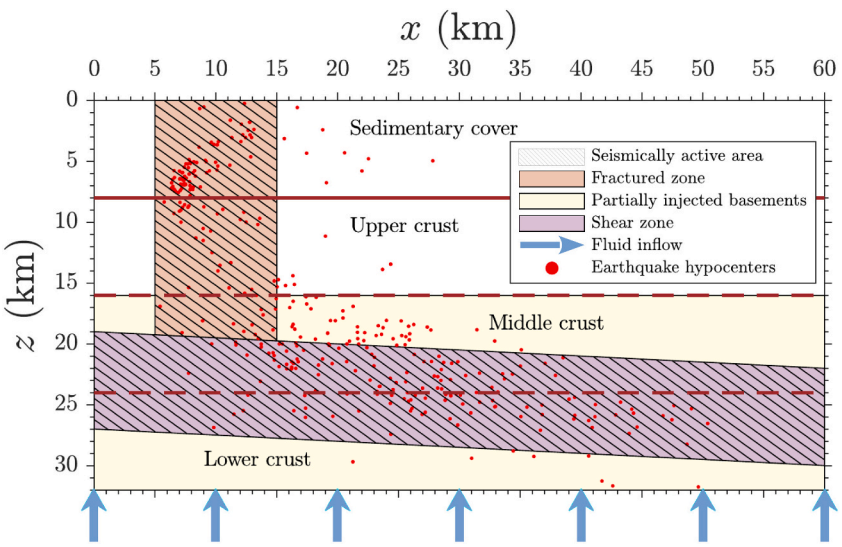

Fig. 8. Conceptual framework for the lithology, tectonic structures and role of fluids for crustal seismicity, illustrated by schematic cross-section of the studied area, inferred from our model. Moho is taken at a depth of 32 km. The presence of fractures and faults affects the sedimentary cover and shallow levels of the crystalline basement. The basement is partly composed of mafic rocks. The fractures can represent favorable intervals for fluid circulation. In proximity of the crustal base, a deep fluid source can provide fluids that collect along shear zones, where porosity is greater than in the surrounding rocks. Hatched areas mark the envelope of the depth distribution of seismicity.

references therein) and surrounding regions referred as CiMACI province. The source of this anorogenic magmatic activity is still a matter of debate, but there is a general consensus on mantle plume components characterizing these rocks (e.g. Lustrino and Wilson, 2007). The mantle plumes which may have contributed to the CiMACI province magmatism are often characterized by modest dimensions and low potential temperature, and are therefore difficult to detect (e.g. Kuritani et al., 2017; Koptev et al., 2021). Given the magmatic history of the GP, we hypotesize that small, local mantle diapiric upwellings or hydrous plumes (e.g. Kuritani et al., 2017, 2019; Cloetingh et al., 2022) could provide volatiles in the lower crust and determine the seismicity that characterizes the area. Obviously, further studies are needed to validate this hypothesis.

Hypocenters beneath the GP show a distribution along a low-angle NE-dipping interval. The orientation of this layer is coherent with regional thrust structures affecting Gargano at shallower depth, generated during middle to upper Miocene NE-SW contractional deformation (Bertotti et al., 1999). Previous studies suggest that aqueous fluids in the continental crust can percolate by porous flow or surface energy-driven infiltration (Watson and Brenan, 1987). These mechanisms are further enhanced along shear zones, where subgrain rotation recrystallization during mylonite formation gives rise to creep cavities (Gilgannon et al., 2020). Therefore, the earthquake hypocenters distribution seems to suggest the presence of one or more pre-existing deep structures, reactivated by present-day tectonics and where fluids can concentrate (Fig. 8). The activity of such structures can be related to phases of viscous deformation alternate to phases of brittle failure, possibly due to events of charge/discharge of fluids. The characteristics of this deep seismogenic structure and its depth makes its interpretation challenging. Thick-skinned tectonics has been invoked for the last compressional phases of the Apennines-foreland system, where deep faulting involving the basement exerts a control over shallower deformation style (Coward et al., 1999, e.g.). This interpretation is opposed to a mode of thin-skinned tectonics, where the base of the Mesozoic sedimentary cover constitutes a detachment level of contractional deformation, superimposed on the older Cretaceous to Tertiary inversion of normal faults (e.g. Scrocca et al., 2007). In a thick-skinned tectonic phase, this seismogenic layer may reflect active strain along a very deep, low-angle detachment level, accommodating deformation that is not detected at surface. Similar foreland inversion tectonics involving the basement occurs in several other regions around the globe (e.g. Roure et al., 2009, and references therein), such as the Atlas domain (Khomsi et al., 2019), Pyrenees (e.g. Odlum et al., 2019) and Tucumán basin (Iaffa et al., 2011). Shear structures that resemble the seismically active structure in the GP has been observed N of the study area, in the central Adriatic upper crust at a depth of 8 km (Finetti and Del Ben, 2005). In contrast, no low-angle structures have been detected in the northern and southern Adriatic basement. Therefore, this structure may represent the deepest detachment level in the Adriatic foreland, that can be generated by an anomalous stress field. Such a scenario may further support the hypothesis of small scale mantle diapirs, generating local strain that is accommodated along a deep detachment level without transfer to shallower depths in the basement and sedimentary cover. Follow-up studies should address open questions on the tectonic setting of the Apulian basement, in particular concerning the characteristics of thick-skinned tectonics phases in the GP and mantle flow beneath the region. This study is focused on a set of data collected in a period of around 8 years on the GP. Although the current model fits well the resulting observations, it could be further tested in future studies, when larger data sets will be available for the seismicity, isostatic movements and relative motion of the GP and Adriatic plate on a broader scale.

6. Conclusions

In our study we present a steady-state thermo-rheological model of the GP region, to assess the effect of temperature, lithology, tectonic variations and fluid presence on crustal rheology and rock strength. This study provides new insight on geophysical observations accounting for the ongoing crustal deformations in the Apennines foreland. Our model provides a novel interpretation of the peculiar seismic pattern and the remarkable differences in heat flow values in the study area. We calculated the temperature, strength distribution and rheology to better comprehend the mechanisms that can lead to a seismic response of the GP crust to deformation. Our findings suggest that the prime conditions for the observed seismicity in the GP lower crust are: presence of fluids at near-lithostatic pressure, low temperatures at the base of the crust and a mafic component in the crystalline basement. Low values of fluid pressure can lead to brittle behavior in shallow levels of the GP crust, but not with the characteristics observed in the region SW of the GP. In addition, a brittle, low-strength lower crust can be generated only by assuming the presence of fluids in the deepest parts of the basement. This is a plausible alternative mechanism for deep seismicity by stress transfer, given the absence of shallow earthquakes and the ductile behavior characterizing the upper basement and lower sedimentary cover in the GP. An improved correspondence between heat flow values, hypocenters distribution and thickness of brittle layers in the lower crust is obtained when temperatures at the base of the model do not exceed 450 °C. The presence of a mafic component in the Apulian basement is

another element that contributes to increase the lower crustal strength, and promotes brittle behavior and a seismogenic response during deformation. Due to the significant depth where fluid presence occurs and the lack of shallow seismicity in the GP, it is likely that the fluid source is located beneath the crust. Taking into account the history of magmatism that characterizes the GP during Paleocene, we hypothesize that fluid sources are located in the mantle and may persist up to the present day. This requires further investigation by studies aimed to resolve the state of the mantle beneath the GP and the Apulian foreland. This can also lead to better insights into rheological characteristics of the lower crust in other areas, especially in the CiMACI province.

The links between stress release, rock deformation and seismic activity are still poorly investigated in the lower crust. Due to the operation of the GSN that records a continuous low energy seismicity, the GP constitutes a fairly unique opportunity for the interpretation of the mechanisms leading to earthquake nucleation in the lower crust. Therefore, further study of the GP can provide valuable keys for interpretation of rheological patterns and seismic activity in other areas, especially where seismicity is triggered by fluid presence and fluid sources are not well identified.

Declaration of Competing Interest

The authors declare that they have no known competing financial interests or personal relationships that could have appeared to influence the work reported in this paper.

Data availability

Data will be made available on request.

Acknowledgement

This study was supported by Project PRIN n. 201743P29 FLUIDS (Detection and tracking of crustal fluid by multi-parametric methodologies and technologies). We are grateful to Prof. A. Caggianelli for stimulating discussions on the composition of the Apulian crystalline basement. We thank S. Miccolis for the realisation of Fig. 1. We thank Prof. F. Roure, Prof. A. Muluneh and Prof. D. Keir for their careful reading of our manuscript and their many insightful comments and suggestions.

Appendix A. Lithologies constituting the crustal layers

In our simulations the rheological behavior of the rocks constituting each layer is calculated on the basis of a polymineralic composition of the GP crust. More in detail, we assume a polyphase composition of each model layer, taking into account the rheological parameters of each mineral and their volume percentage in the rocks. The mineral assemblage and the volume percentage of minerals composing the layers are based on average compositions for the lithologies occurring in the GP (e.g. Philpotts and Ague, 2009) and are illustrated in Table 2.

1. Carbonate rocks (limestone and dolostone), locally interbedded with chert layers, with age ranging between upper Jurassic and Eocene. These rocks are by far the most common lithologies outcropping in the GP. Locally they can be covered by Quaternary sediments, that are discontinuous and with modest thickness and are not incorporated in the simulations.
2. Anhydrite, limestones and dolostones, corresponding to the Anidriti di Burano formation. These rocks have upper Triassic age (Carnian-Rhaetian) and variable thickness.
3. Permo-Triassic clastic continental rocks. In the lowermost part, this formation is constituted by low degree phyllites, with possible presence of intrusive bodies.
4. Upper crust phyllites, micaschists and paragneisses with intercalate metavolcanic rocks and marbles.
5. Carboniferous plutonic rocks with composition varying from granite to granodiorite and tonalite. Peralouminous rocks are present, as well as aluminosilicates.
6. Granulite-facies metapelites and migmatites, with alouminous paragneiss and minor metabasites and metacarbonatic rocks. In the upper part, the granulite rocks show an overprint under amphibolite-facies conditions.

The Anidriti di Burano and the Permo-Triassic rocks have been drilled by two wells in the Murge area (Puglia 1 well, Patacca and Scandone, 2007) and in the Northern GP (Gargano 1 well, Bosellini and Morsilli, 2001, and references therein). In addition, the Sannicandro 1 well reached a thick succession of anhydrite and dolostone being part of the Anidriti di Burano formation. These thick Paleozoic and Triassic formations have also been detected in the southern (Patacca and Scandone, 2007) and central Apennines (Patacca et al., 2008). Diapirism of the Anidriti di Burano formation has been detected in proximity of the Punta delle Pietre Nere outcrop (Festa et al., 2019), as well as the adjacent region of the Tremiti Islands (Festa et al., 2014; Teofilo et al., 2016) and central Adriatic (Scrocca et al., 2007). However, there is no other evidence of diapirs in other sectors of the GP, therefore the formation has been modeled as horizontal in our simulations. Based of the available data in the GP and surrounding regions, the presence of the Anidriti di Burano formation does not lead to any anomaly in heat flow, irrespective of the structural relationships with adjacent rocks. This is a remarkable difference with respect to other areas where the high values of thermal conductivity of evaporites produces thermal anomalies (Guillou-Frottier et al., 2010; Bonté et al., 2012, e.g.), and may be due to the variable, locally high fraction of dolostone embedded in the formation, as shown in the Gargano 1 and Foresta Umbra 1 wells (Bosellini and Morsilli, 2001, and references therein). In some of the simulations (case F and G and Appendix C, Fig. C.1), we tested the rheological effect that the presence of mafic rocks can exert on the basement. This has been done by adopting a mineral assemblage for the middle and lower crust composed of gabbro for a volume percentage up to 35% vol., and the remaining volume constituted by the lithologies described above.

Appendix B. Procedure followed to develop the model

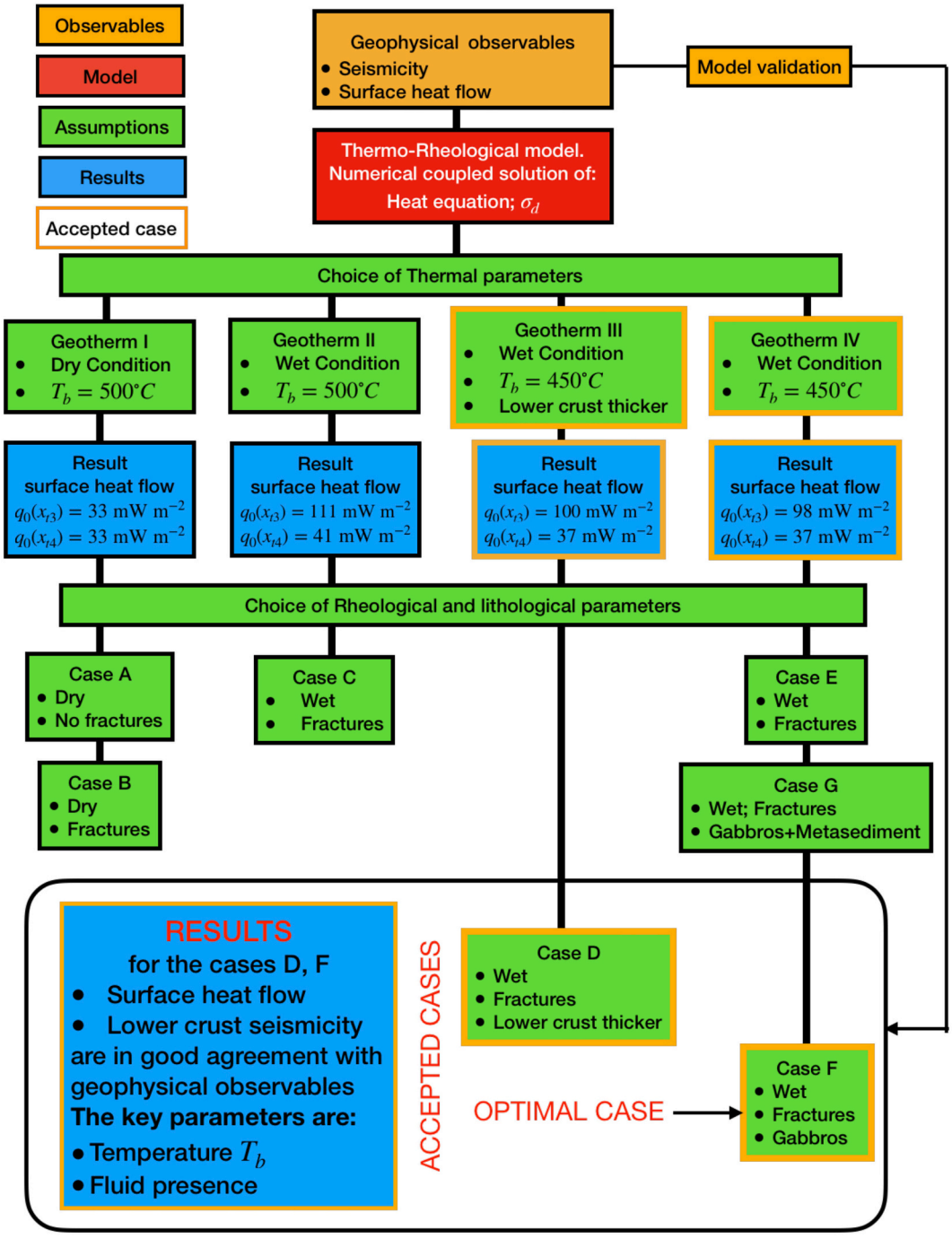

Fig. B.1. Flow chart summarizing the procedure followed to develop the model.

Appendix C. Crustal rheology $R_h(x,z)$ and effect of S and λ on σ_d

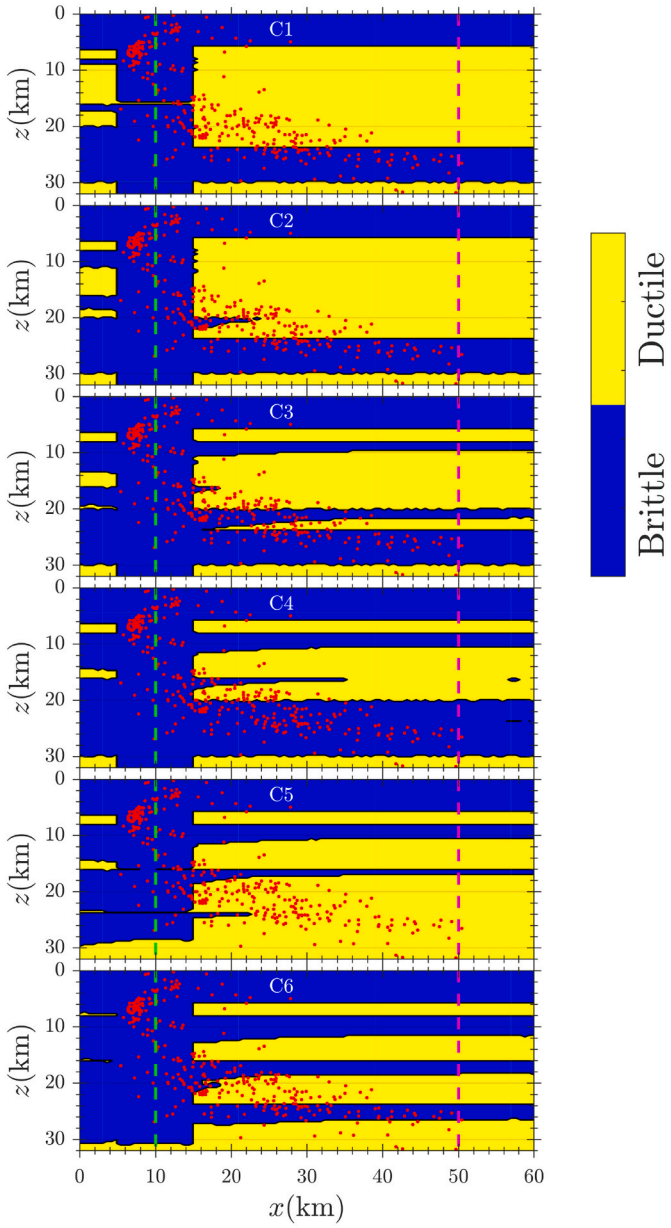

Fig. C.1. Crustal rheology $R_h(x,z)$ in addition to the cases shown in Figs. 3–6 in the main text. Mafic material is intruded in the entire crystalline basement for different volume percentages: C1 10%, C2 20%, C3 30%, C4-C6 35%. For C5 and C6 dry condition is considered with $\lambda = 0.4$ in the entire crust. In C6 a strain rate $\dot{\varepsilon} = 10^{-13}$ s^{-1} is adopted. All other parameters are given in Tables 1, 2.

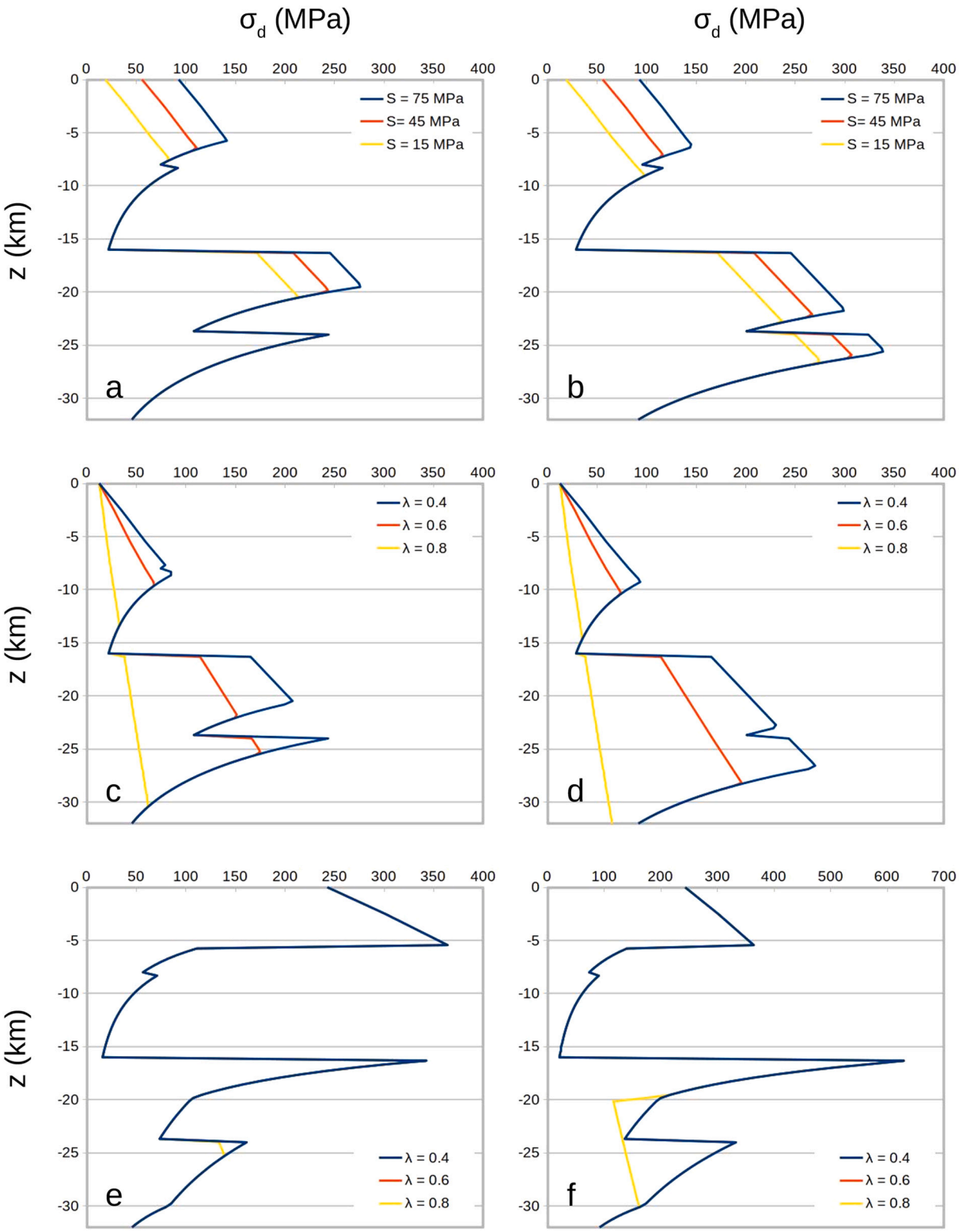

Fig. C.2. σ_d versus z plots for simulations where the lower and middle crust are composed of mafic rocks with a percentage of 35% vol. Panels a, b, c and d are for $x = x_{t3}$ while panels e and f are for $x = x_{t4}$ (see Fig. 2). The adopted parameters are: a) $T_b = 500$°C, $\lambda = 0.4$; b) $T_b = 450$°C, $\lambda = 0.4$; c and e) $T_b = 500$°C, $S = 10$ MPa; d and f) $T_b = 450$°C, $S = 10$ MPa.

References

Aldersons, F., Ben-Avraham, Z., Hofstetter, A., Kissling, E., Al-Yazjeen, T., 2003. Lower-crustal strength under the Dead Sea basin from local earthquake data and rheological modeling. Earth Planet. Sci. Lett. 214, 129–142. https://doi.org/10.1016/S0012-821X(03)00381-9.

Aliaj, S., 2006. The Albanian Orogen: Convergence Zone between Eurasia and the Adria Microplate. In: Pinter, N., Gyula, G., Weber, J., Stein, S., Medak, D. (Eds.), The Adria Microplate: GPS Geodesy, Tectonics and Hazards, Springer Netherlands, Dordrecht, pp. 133–149.

Amato, A., Bianchi, I., Agostinetti, N., 2014. Apulian crust: top to bottom. J. Geodyn. 82, 125–137.

Anikiev, D., Cacace, M., Bott, J., Gomez Dacal, M., Scheck-Wenderoth, M., 2020. Influence of lithosphere rheology on seismicity in an intracontinental rift: the case of the Rhine Graben. Front. Earth Sci. 8, 592561 https://doi.org/10.3389/feart.2020.592561.

Argnani, A., Rovere, M., Bonazzi, C., 2009. Tectonics of the Mattinata fault, offshore south Gargano (southern Adriatic Sea, Italy): Implications for active deformation and seismotectonics in the foreland of the Southern Apennines. Bull. Geol. Soc. Am. 121, 1421–1440.

Audin, L., Avouac, J.P., Flouzat, M., Plantet, J.L., 2002. Fluid-driven seismicity in a stable tectonic context: the Remiremont fault zone, Vosges, France. Geophys. Res. Lett. 29 https://doi.org/10.1029/2001GL012988.

Babbucci, D., Tamburelli, C., Viti, M., Mantovani, E., Albarello, D., D'Onza, F., Cenni, N., Mugnaioli, E., 2004. Relative motion of the Adriatic with respect to the confining plates: Seismological and geodetic constraints. Geophys. J. Int. 159, 765–775.

Balfour, N., Cummins, P., Pilia, S., Love, D., 2015. Localization of intraplate deformation through fluid-assisted faulting in the Lower-Crust: the Flinders Ranges, South Australia. Tectonophysics 655. https://doi.org/10.1016/j.tecto.2015.05.014.

Battaglia, M., Murray, M., Serpelloni, E., Burgmann, R., 2004. The Adriatic region: an independent microplate within the Africa-Eurasia collision zone. Geophys. Res. Lett. 31. L09605 1–4.

Benson, P., Austria, D., Gehne, S., Butcher, E., Harnett, C., Fazio, M., Rowley, P., Tomas, R., 2020. Laboratory simulations of fluid-induced seismicity, hydraulic fracture, and fluid flow. Geomech. Energy Environ. 24 https://doi.org/10.1016/j.gete.2019.100169.

Bertotti, G., Casolari, E., Picotti, V., 1999. The gargano promontory: a neogene contractional belt within the Adriatic plate. Terra Nova 11, 168–173.

Bertotti, G., Picotti, V., Chilovi, C., Fantoni, R., Merlini, S., Mosconi, A., 2001. Neogene to Quaternary sedimentary basins in the south Adriatic (Central Mediterranean): Foredeeps and lithospheric buckling. Tectonics 20 (5), 771–787. https://doi.org/10.1029/2001TC900012.

Bigazzi, G., Laurenzi, M., Principe, C., D, B., 1996. New geochronological data on igneous rocks and evaporites of the Pietre Nere Point (Gargano peninsula, southern Italy). Boll. Soc. Geol. Ital. 115, 439–448.

Bonté, G., van Wees, J.-D., Verweij, J., 2012. Subsurface temperature of the onshore Netherlands: new temperature dataset and modeling. Neth. J. Geosci. 91 (4) https://doi.org/10.1017/S00167746000003545.

Bosellini, A., Morsilli, M., 2001. Il Promontorio del Gargano: cenni di geologia e itinerari geologici. Quad. Parco Naz. Gargano. https://doi.org/10.13140/RG.2.1.2715.3360.

Brankman, C., Aydin, A., 2004. Uplift and contractional deformation along a segmented strike-slip fault system: the Gargano Promontory, southern Italy. J. Struct. Geol. 26, 807–824.

Burov, E.B., 2011. Rheology and strength of the lithosphere. Mar. Pet. Geol. 28, 1402–1443. https://doi.org/10.1016/j.marpetgeo.2011.05.008.

Byrelee, J., 1992. The change in orientation of subsidiary shears near faults containing pore fluid under high pressure. Tectonophysics 211 (1–4), 295–303. https://doi.org/10.1016/0040-1951(92)90066-F.

Campbell, L., Menegon, L., Fagereng, Å., Pennacchioni, G., 2020. Earthquake nucleation in the lower crust by local stress amplification. Nat. Commun. 11.

Carmichael, R., 2017. Handbook of Physical Properties of Rocks (1982), Vol. II. CRC Press Revivals, CRC Press.

Cecere, G., 2018. III relazione 2018 all'accordo tra regione Puglia sezione Protezione Civile e l'Istituto Nazionale di Geofisica e Vulcanologia (INGV) per il supporto alle attività di protezione civile connesse con il rischio sismico "Informazione rapida per la gestione delle emergenze sismiche".

Chen, W.P., Molnar, P., 1983. Focal depths of intracontinental and intraplate earthquakes and their implications for the thermal and mechanical properties of the lithosphere. J. Geophys. Res. Solid Earth 88, 4183–4214.

Chen, Q., Nur, A., 1992. Pore fluid pressure effects in anisotropic rocks: Mechanisms of induced seismicity and weak faults. Pure Appl. Geophys. PAGEOPH 139, 463–479. https://doi.org/10.1007/BF00879947.

Chernak, L., Hirth, G., Selverstone, J., Tullis, J., 2009. Effect of aqueous and carbonic fluids on the dislocation creep strength of quartz. J. Geophys. Res. 114, B04201. https://doi.org/10.1029/2008JB005884.

Clauser, C., Huenges, E., 1995. Thermal conductivity of rocks and minerals. Am. Geophys. Union (AGU). 105–126.

Cloetingh, S., Burov, E., 1996. Thermomechanical structure of European continental lithosphere: Constraints from rheological profiles and EET estimates. Geophys. J. Int. 124, 695–723.

Cloetingh, S., Burov, E., 2011. Lithospheric folding and sedimentary basin evolution: a review and analysis of formation mechanisms. Basin Res. 23, 257–290. https://doi.org/10.1111/j.1365-2117.2010.00490.x.

Cloetingh, S., Koptev, A., Lavecchia, A., Kovacs, I., Beekman, F., 2022. Fingerprinting secondary mantle plumes. In: Accepted for publication in Earth and Planetary Science Letters.

Coward, M., De Donatis, M., Mazzoli, S., Paltrinieri, W., Wezel, F., 1999. Frontal part of the northern Apennines fold and thrust belt in the Romagna-Marche area (Italy): Shallow and deep structural styles. Tectonics 18, 559–574. https://doi.org/10.1029/1999TC900003.

Craig, T., Jackson, J., 2021. Variations in the seismogenic thickness of East Africa. J. Geophys. Res. 126, e2020JB020754 https://doi.org/10.1029/2020JB020754.

D'Agostino, N., Avallone, A., Cheloni, D., D'Anastasio, E., Mantenuto, S., Selvaggi, G., 2008. Active tectonics of the Adriatic region from GPS and earthquake slip vectors. Journal of Geophysical Research: Solid. Earth 113.

De Fino, M., La Volpe, L., Piccarreta, G., 1981. Geochemistry and petrogenesis of the Paleocene platform magmatism at Punta delle Pietre Nere (southeastern Italy). Neues Jahrbuch fur Mineralogie, Abhandlungen 142, 161–177.

de Lorenzo, S., Michele, M., Emolo, A., Tallarico, A., 2017. A 1D P-wave velocity model of the Gargano promontory (South-Eastern Italy). J. Seismol. 21, 909–919. https://doi.org/10.1007/s10950-017-9643-7.

Deichmann, N., 1992. Structural and rheological implications of lower-crustal earthquakes below northern Switzerland. Phys. Earth Planet. Inter. 69, 270–280.

Del Gaudio, V., Pierri, P., Frepoli, A., Calcagnile, G., Venisti, N., Cimini, G., 2007. A critical revision of the seismicity of Northern Apulia (Adriatic microplate - Southern Italy) and implicationsfor the identification of seismogenic structures. Tectonophysics 436, 9–35.

Della Vedova, B., Bellani, S., Pellis, G., Squarci, P., 2001. Deep Temperatures and Surface Heat Flow Distribution. Springer, Netherlands, Dordrecht, pp. 65–76.

Déverchère, J., Petit, C., Gileva, N., Radziminovitch, N., Melnikova, V., San'Kov, V., 2001. Depth distribution of earthquakes in the Baikal rift system and its implications for the rheology of the lithosphere. Geophys. J. Int. 146, 714–730.

Dragoni, M., Doglioni, C., Mongelli, F., Zito, G., 1996. Evaluation of stresses in two geodynamically different areas: Stable foreland and extensional backarc. Pure Appl. Geophys. 146, 319–341.

El Hariri, M., Abercrombie, R., Rowe, C., do Nascimento, A., 2010. The role of fluids in triggering earthquakes: Observations from reservoir induced seismicity in Brazil. Geophys. J. Int. 181, 1566–1574. https://doi.org/10.1111/j.1365-246X.2010.04554.x.

Fagereng, Å., Biggs, J., 2019. New perspectives on 'geological strain rates' calculated from both naturally deformed and actively deforming rocks. J. Struct. Geol. 125, 100–110. https://doi.org/10.1016/j.jsg.2018.10.004.

Festa, V., Fregola, R., Acquafredda, P., De Giosa, F., Monno, A., Ventruti, G., 2019. The enigmatic ascent of Ca-sulphate rocks from a deep dense source layer: evidences of hydration diapirism in the Lesina Marina area (Apulia, southern Italy). Int. J. Earth Sci. 108, 1897–1912. https://doi.org/10.1007/s00531-019-01739-1.

Festa, V., Teofilo, G., Tropeano, M., Sabato, L., Spalluto, L., 2014. New insights on diapirism in the Adriatic Sea:the Tremiti salt structure (Apulia offshore, southeastern Italy). Terra Nova 26, 169–181. https://doi.org/10.1111/ter.12082.

Filippucci, M., Del Pezzo, E., de Lorenzo, S., Tallarico, A., 2019a. 2D kernel-based imaging of coda-Q space variations in the Gargano Promontory (Southern Italy). Phys. Earth Planet. Inter. 297, 106313 https://doi.org/10.1016/j.pepi.2019.106313.

Filippucci, M., Tallarico, A., Dragoni, M., de Lorenzo, S., 2019b. Relationship between depth of seismicity and heat flow: the case of the gargano area (Italy). Pure Appl. Geophys. 176, 2383–2394. https://doi.org/10.1007/s00024-019-02107-5.

Filippucci, M., Pierri, P., de Lorenzo, S., Tallarico, A., 2020. The stress field in the northern apulia (Southern Italy), as deduced from microearthquake focal mechanisms: new insight from local seismic monitoring. In: Lecture Notes in Computer Science (including subseries Lecture Notes in Artificial Intelligence and Lecture Notes in Bioinformatics) 12255 LNCS, pp. 914–927. https://doi.org/10.1007/978-3-030-58820-5_66.

Filippucci, M., Lucente, S., Del Pezzo, E., de Lorenzo, S., Prosser, G., Tallarico, A., 2021a. 3d-kernel based imaging of an improved estimation of (Qc) in the northern apulia (southern Italy). Appl. Sci. (Switzerland) 11 (16), 7512. https://doi.org/10.3390/app11167512.

Filippucci, M., Miccolis, S., Castagnozzi, A., Cecere, G., de Lorenzo, S., Donvito, G., Falco, L., Michele, M., Nicotri, S., Romeo, A., Selvaggi, G., Tallarico, A., 2021b. Seismicity of the Gargano promontory (Southern Italy) after 7 years of local seismic network operation: Data release of waveforms from 2013 to 2018. Data Brief 35, 106783. https://doi.org/10.1016/j.dib.2021.106783.

Finetti, I., Del Ben, A., 2005. Crustal Tectono-Stratigraphic Setting of the Adriatic Sea from New CROP Seismic Data, vol. 1. Elsevier, Amsterdam, pp. 519–548.

Gao, Z., Wang, K., 2017. Rheological separation of the megathrust seismogenic zone and episodic tremor and slip. Nature 543, 416–419. https://doi.org/10.1038/nature21389.

Gardonio, B., Jolivet, R., Calais, E., Leclère, H., 2018. The April 2017 Mw6.5 botswana earthquake: an intraplate event triggered by deep fluids. Geophys. Res. Lett. 45, 8886–8896.

Gerya, T., 2009. Numerical Solution of the Heat Conservation Equation. Cambridge University Press, pp. 133–148.

Gilgannon, J., Poulet, T., Berger, A., Barnhoorn, A., Herwegh, M., 2020. Dynamic recrystallization can produce porosity in shear zones. Geophys. Res. Lett. 47.

Girard, J., Chen, J., Raterron, P., Holyoke, C., 2013. Hydrolytic weakening of olivine at mantle pressure: evidence of [100](010) slip system softening from single-crystal deformation experiments. Phys. Earth Planet. Inter. 216, 12–20. https://doi.org/10.1016/j.pepi.2012.10.009.

Gruber, B., Chacko, T., Pearson, D., Currie, C., Menzies, A., 2021. Heat production and moho temperatures in cratonic crust: evidence from lower crustal xenoliths from the slave craton. Lithos 380-381. https://doi.org/10.1016/j.lithos.2020.105889.

Guillou-Frottier, L., Lucazeau, F., Garibaldi, C., Bonté, D., Coueffe, R., 2010. Heat flow and deep temperatures in the Southeast Basin of France: implications for local

rheological contrasts. Bull. Soc. Geol. Fr. 181 (6), 531–546. https://doi.org/10.2113/gssgfbull.181.6.531.
Hecht, F., 2012. New development in freefem+. J. Numer. Math. 20, 251–265.
Heidbach, O., Rajabi, M., Reiter, K., Ziegler, M.O., 2019. World Stress Map. Springer International Publishing, Cham, pp. 1–8.
Hofstetter, R., Dorbath, C., Caló, M., 2012. Crustal structure of the Dead Sea Basin from local earthquake tomography. Geophys. J. Int. 189 (1), 554–568. https://doi.org/10.1111/j.1365-246X.2012.05369.x.
Iaffa, D., Sabat, F., Bello, D., Ferrer, O., Mon, R., Gutierrez, A., 2011. Tectonic inversion in a segmented foreland basin from extensional to piggy back settings: the Tucumán basin in NW Argentina. J. S. Am. Earth Sci. 31, 457–474. https://doi.org/10.1016/j.jsames.2011.02.009.
Iio, Y., Sagiya, T., Kobayashi, Y., Shiozaki, I., 2002. Water-weakened lower crust and its role in the concentrated deformation in the Japanese Islands. Earth Planet. Sci. Lett. 203, 245–253.
Improta, L., De Gori, P., Chiarabba, C., 2014. New insights into crustal structure, Cenozoic magmatism, CO_2 degassing, and seismogenesis in the southern Apennines and Irpinia region from local earthquake tomography. J. Geophys. Res. Solid Earth 119, 8283–8311.
Jamtveit, B., Ben-Zion, Y., Renard, F., Austrheim, H., 2018. Earthquake-induced transformation of the lower crust. Nature 556, 487–491.
Jamtveit, B., Petley-Ragan, A., Incel, S., Dunkel, K., Aupart, C., Austrheim, H., Corfu, F., Menegon, L., Renard, F., 2019. The effects of earthquakes and fluids on the metamorphism of the lower continental crust. J. Geophys. Res. Solid Earth 124, 7725–7755. https://doi.org/10.1029/2018JB016461.
Ji, S., Zhao, P., Xia, B., 2003. Flow laws of multiphase materials and rocks from end-member flow laws. Tectonophysics 370, 129–145.
Khomsi, S., Roure, F., Khelil, M., Mezni, R., Echihi, O., 2019. A review of the crustal architecture and related pre-salt oil/gas objectives of the eastern Maghreb Atlas and tell: need for deep seismic reflection profiling. Tectonophysics 766, 232–248. https://doi.org/10.1016/j.tecto.2019.06.009.
Koptev, A., Cloetingh, S., Ehlers, T., 2021. Longevity of small-scale (baby) plumes and their role in lithospheric break-up. Geophys. J. Int. 227, 439–471.
Kuritani, T., Sakuyama, T., Kamada, N., Yokoyama, T., Nakagawa, M., 2017. Fluid-fluxed melting of mantle versus decompression melting of hydrous mantle plume as the cause of intraplate magmatism over a stagnant slab: Implications from Fukue Volcano Group, SW Japan. Lithos 282-283, 98–110.
Kuritani, T., Xia, Q., Kimura, J., Liu, J., Shimizu, K., Ushikubo, T., Zhao, D., Nakagawa, M., Yoshimura, S., 2019. Buoyant hydrous mantle plume from the mantle transition zone. Nat. Sci. Rep. 9, 6549. https://doi.org/10.1038/s41598-019-43103-y.
Lavecchia, A., Clark, S., Beekman, F., Cloetingh, S., Burov, E., 2016. Thermal perturbation, mineral assemblages, and rheology variations induced by dyke emplacement in the crust. Tectonics 35, 1137–1152.
Lenkey, L., P, D., Horvath, F., Cloetingh, S., 2002. Geothermics of the Pannonian basin and its bearing on the neotectonics. Stephan Mueller Special Publication Series 3.
Loddo, M., Quarto, R., Schiavone, D., 1996. Integrated geophysical survey for the geological structural and hydrogeothermal study of the North-western Gargano promontory (Southern Italy). Ann. Geofis. 39, 201–219.
Lustrino, M., Wilson, M., 2007. The circum-Mediterranean anorogenic Cenozoic igneous province. Earth Sci. Rev. 81, 1–65.
Mazzeo, F., Arienzo, I., Aulinas, M., Casalini, M., Di Renzo, V., D'Antonio, M., 2018. Mineralogical, geochemical and isotopic characteristics of alkaline mafic igneous rocks from Punta delle Pietre Nere (Gargano, Southern Italy). Lithos 308-309, 316–328.
Meissner, R., Kern, H., 2008. Earthquakes and strength in the laminated lower crust -Can they be explained by the "corset model"? Tectonophysics 448, 49–59. https://doi.org/10.1016/j.tecto.2007.11.034.
Menegon, L., Fusseis, F., Stünitz, H., Xiao, X., 2015. Creep cavitation bands control porosity and fluid flow in lower crustal shear zones. Geology 43, 227–230. https://doi.org/10.1130/G36307.1.
Miccolis, S., Filippucci, M., de Lorenzo, S., Frepoli, A., Pierri, P., 2021. Seismogenic structures orientation and stress field of the Gargano Promontory (southern Italy) from microseismicity analysis. Front. Earth Sci. 9, 589332 https://doi.org/10.3389/feart.2021.589332.
Morsili, M., 2016. Sintesi delle conoscenze geologiche e stratigra che del Promontorio del Gargano. Geol. Terr. 3, 15–30.
Muluneh, A., Keri, D., Corti, G., 2021. Thermo-rheological properties of the Ethiopian lithosphere and evidence for transient fluid induced lower crustal seismicity beneath the Ethiopian rift. Front. Earth Sci. 9, 610165 https://doi.org/10.3389/feart.2021.610165.
Neely, J.S., Stein, S., 2021. Why do continental normal fault earthquakes have smaller maximum magnitudes? Tectonophysics 809, 228854. https://doi.org/10.1016/j.tecto.2021.228854.
Noda, H., Dunham, E., Rice, J., 2009. Earthquake ruptures with thermal weakening and the operation of major faults at low overall stress levels. J. Geophys. Res. Solid Earth 114. https://doi.org/10.1029/2008JB006143.
Odlum, M., Stockli, D., Capaldi, T., Thomson, K., Clark, J., Puigdefabregas, C., Fildani, A., 2019. Tectonic and sediment provenance evolution of the South Eastern Pyrenean foreland basins during rift margin inversion and orogenic uplift. Tectonophysics 765, 226–248. https://doi.org/10.1016/j.tecto.2019.05.008.
Oldow, J., Ferranti, L., Lewis, D., Campbell, J., D'Argenio, B., Catalano, R., Pappone, G., Carmignani, L., Conti, P., Aiken, C., 2002. Active fragmentation of Adria, the north African promontory, Central Mediterranean orogen. Geology 30, 779–782.
Pasquale, V., Cabella, C., Verdoya, M., 1990. Deep temperatures and lithospheric thickness along the European Geotraverse. Tectonophysics 176, 1–11. https://doi.org/10.1016/0040-1951(90)90255-7.
Patacca, E., Scandone, P., 2007. Geological interpretation of the CROP-04 seismic line (Southern Apennines, Italy). Boll. Soc. Geol. Special Issue 7, 297–315.
Patacca, E., Scandone, P., Di Luzio, E., Cavinato, G., Parotto, M., 2008. Structural architecture of the central Apennines: interpretation of the CROP 11 seismic profile from the Adriatic coast to the orographic divide. Tectonics 27 (TC3006). https://doi.org/10.1029/2005TC001917.
Philpotts, A., Ague, J., 2009. Principles of Igneous and Metamorphic Petrology, 2 ed. Cambridge University Press. https://doi.org/10.1017/CBO9780511813429.
Radziminovich, N., Gileva, N., Melnikova, V., Ochkovskaya, M., 2013. Seismicity of the Baikal rift system from regional network observations. J. Asian Earth Sci. 62, 146–161. https://doi.org/10.1016/j.jseaes.2012.10.029.
Ranalli, G., 1995. Rheology of the Earth. Chapman and Hall, London, U.K.
Roure, F., Nazaj, S., Mushka, K., Fili, I., Cadet, J., Bonneau, M., 2004. Kinematic evolution and petroleum systems: An appraisal of the Outer Albanides, in Thrust Tectonics and Hydrocarbon Systems. In: McClay, K. (Ed.), Thrust Tectonics and Hydrocarbon Systems. AAPG memoir, Tulsa, Oklahoma, pp. 474–493.
Roure, F., Swennen, R., Schneider, F., Faure, J., Ferket, H., Guilhaumou, N., Osadetz, K., Robion, P., Vandeginste, V., 2005. Incidence and importance of tectonics and natural fluid migration on reservoir evolution in foreland fold-and-thrust belts. Oil Gas Sci. Technol.- Revue de l IFP 60, 67–106. https://doi.org/10.2516/ogst:2005006.
Roure, F., Cloetingh, S., Scheck-Wenderoth, M., Ziegler, P., 2009. Achievements and challenges in sedimentary basin dynamics: a review. In: Cloetingh, S., Negendank, J. (Eds.), New Frontiers in Integrated Solid Earth Sciences. International Year of Planet Earth, Springer, Dordrecht. https://doi.org/10.1007/978-90-481-2737-5_5.
Ranalli, G., Murphy, D., 1987. Rheological stratification of the lithosphere. Tectonophysics 132 (4), 281–295. https://doi.org/10.1016/0040-1951(87)90348-9.
Roure, F., Casero, P., Addoum, B., 2012. Alpine inversion of the North African margin and delamination of its continental lithosphere. Tectonics 31, TC3006. https://doi.org/10.1029/2011TC002989.
Rovida, A., Locati, M., Camassi, R., Lolli, B., Gasperini, P., 2019. Catalogo Parametrico dei Terremoti Italiani, CPTI15 versione 2.0.
Salamon, A., Hofstetter, A., Garfunkel, Z., Ron, H., 2003. Seismotectonics of the Sinai subplate - the eastern Mediterranean region. Geophys. J. Int. 155, 149–173.
Schenk, V., 1981. Synchronous uplift of the lower crust of the Ivrea Zone and of Southern Calabria and its possible consequences for the Hercynian orogeny in Southern Europe. Earth Planet. Sci. Lett. 56, 305–320.
Schutt, D., Lowry, A., Buehler, J., 2018. Moho temperature and mobility of lower crust in the western United States. Geology 46, 219–222. https://doi.org/10.1130/G39507.1.
Scrocca, D., Carminati, E., Doglioni, C., Marcantoni, D., 2007. Slab retreat and active shortening along the Central-Northern Apennines. In: Lacombe, O., Roure, F., Lavé, F., Vergés, J. (Eds.), Thrust Belts and Foreland Basins. Springer, Berlin. https://doi.org/10.1007/978-3-540-69426-7_25.
Shudofsky, G., Cloetingh, S., Stein, S., Wortel, R., 1987. Unusually deep earthquakes in East Africa: Constraints on the thermo-mechanical structure of a continental rift system. Geophys. Res. Lett. 14, 741–744.
Simpson, F., 1999. Stress and seismicity in the lower continental crust: a challenge to simple ductility and implications for electrical conductivity mechanisms. Surv. Geophys. 20, 201–227.
Smith, S., Faulkner, D., 2010. Laboratory measurements of the frictional properties of the Zuccale low-angle normal fault, Elba Island, Italy. Journal of Geophysical Research: Solid. Earth 115.
Stein, S., Sella, G.F., 2006. Pleistocene change from convergence to extension in the Apennines as a consequence of Adria microplate motion. In: Pinter, N., Gyula, G., Weber, J., Stein, S., Medak, D. (Eds.), The Adria Microplate: GPS Geodesy, Tectonics and Hazards. Springer Netherlands, Dordrecht, pp. 21–34.
Tassis, G., Grigoriadis, V., Tziavos, I., Tsokas, G., Papazachos, C., Vasiljević, I., 2013. A new Bouguer gravity anomaly field for the Adriatic Sea and its application for the study of the crustal and upper mantle structure. J. Geodyn. 66, 38–52.
Teofilo, G., Festa, V., Sabato, L., Spalluto, L., Tropeano, M., 2016. 3D modelling of the Tremiti salt diapir in the Gargano offshore (Adriatic Sea, southern Italy): constraints on the Tremiti Structure development. Ita. J. Geosci. 135 (3), 474–485. https://doi.org/10.3301/IJG.2015.40.
Tripaldi, S., 2020. Electrical signatures of a permeable zone in carbonates hosting local geothermal manifestations: Insights for the deep fluid flow in the Gargano area (South-eastern Italy). Boll. Geofis. Teor. Appl. 61 (2), 219–232 doi:doi.org/10.4430/bgta0312.
Tullis, J., Yund, R., 1989. Hydrolytic weakening of quartz aggregates: the effects of water and pressure on recovery. Geophys. Res. Lett. 16, 1343–1346. https://doi.org/10.1029/GL016i011p01343.
Van Dinther, Y., Gerya, T., Dalguer, L., Mai, P., Morra, G., Giardini, D., 2013. The seismic cycle at subduction thrusts: Insights from seismo-thermo- mechanical models. J. Geophys. Res. Solid Earth 118, 6183–6202.
Wang, Z., Shi, F., Zhang, J., 2020. Effects of water on the rheology of dominant minerals and rocks in the continental lower crust: a review. J. Earth Sci. 31, 1170–1182. https://doi.org/10.1007/s12583-020-1307-9.
Watson, E., Brenan, J., 1987. Fluids in the lithosphere, 1. Experimentally-determined wetting characteristics of CO2 H2O fluids and their implications for fluid transport, host-rock physical properties, and fluid inclusion formation. Earth Planet. Sci. Lett. 85, 497–515.

Winter, T., Tapponnier, P., 1991. Post-Jurassic-pre-Miocene major extension in central Italy; microtectonic evidence [Extension majeure post-Jurassique et ante-Miocene dans le centre de l'Italie: donnees microtectoniques]. Bull. Soc. Geol. Fr. 162, 1095–1108.

Yin, Z.M., Ranalli, G., 1992. Critical stress difference, fault orientation and slip direction in anisotropic rocks under non-Andersonian stress systems. J. Struct. Geol. 14, 237–244.

Zencher, F., Bonafede, M., Stefansson, R., 2006. Near-lithostatic pore pressure at seismogenic depths: a thermoporoelastic model. Geophys. J. Int. 166 (3), 1318–1334. https://doi.org/10.1111/j.1365-246X.2006.03069.x.

Ziegler, P., Cloetingh, S., van Wees, J.-D., 1995. Dynamics of intra-plate compressional deformation: the Alpine foreland and other examples. Tectonophysics 252, 7–59.

Ziegler, P., van Wees, J.-D., Cloetingh, S., 1998. Mechanical controls on collision-related compressional intraplate deformation. Tectonophysics 300, 103–129.